Natural Resources Canada | Ressources naturelles Canada

GEOLOGICAL SURVEY OF CANADA
OPEN FILE 7727

Geology, geochronology, mineral chemistry, and geochemistry: Supporting databases for the convergent margin Ni-Cu-PGE deposit study, Giant Mascot magmatic sulphide deposit, Hope, southwestern British Columbia

M.J. Manor, J.S. Scoates, G.T. Nixon, and D.E. Ames

2015

Canada

GEOLOGICAL SURVEY OF CANADA
OPEN FILE 7727

Geology, geochronology, mineral chemistry, and geochemistry: Supporting databases for the convergent margin Ni-Cu-PGE deposit study, Giant Mascot magmatic sulphide deposit, Hope, southwestern British Columbia

M.J. Manor[1], J.S. Scoates[1], G.T. Nixon[2], and D.E. Ames[3]

[1]Pacific Centre for Isotopic and Geochemical Research, University of British Columbia, Vancouver, British Columbia
[2]British Columbia Geological Survey, Victoria, British Columbia
[3]Geological Survey of Canada, Ottawa, Ontario

2015

doi:10.4095/297318

This publication is available for free download through GEOSCAN (http://geoscan.nrcan.gc.ca/)

Recommended citation

Manor, M.J., Scoates, J.S., Nixon, G.T., and Ames, D.E., 2015. Geology, geochronology, mineral chemistry, and geochemistry: Supporting databases for the convergent margin Ni-Cu-PGE deposit study, Giant Mascot magmatic sulphide deposit, Hope, southwestern British Columbia; Geological Survey of Canada, Open File 7727, 1 zip file. doi:10.4095/297318

Publications in this series have not been edited; they are released as submitted by the author.

Contribution to the Geological Survey of Canada's Targeted Geoscience Initiative 4 (TGI-4) Program (2010-2015)

TABLE OF CONTENTS

Figures

Tables

Geology, geochronology, mineral chemistry, and geochemistry: Supporting databases for the convergent margin Ni-Cu-PGE deposit study, Giant Mascot magmatic sulphide deposit, Hope, southwestern British Columbia

M.J. Manor[1], J.S. Scoates[1], G.T. Nixon[2], and D.E. Ames[3]

[1]Pacific Centre for Isotopic and Geochemical Research, Department of Earth, Ocean and Atmospheric Sciences, University of British Columbia, 6339 Stores Road, Vancouver, British Columbia V6T 1Z4
[2]British Columbia Ministry of Energy and Mines, British Columbia Geological Survey, PO Box 9333 Stn Prov Govt, Victoria, British Columbia V8W 9N3
[3]Geological Survey of Canada, 601 Booth Street, Ottawa, Ontario K1A 0E8

BACKGROUND

Conventionally, convergent margin environments are considered poor targets for Ni-Cu-PGE mineralization due to the apparent lack of ultramafic bodies containing economic Ni-sulphides (Ripley, 2010). Convergent margin Ni-Cu-PGE deposits are, however, becoming an increasingly important economic resource and attractive exploration target globally (e.g. Aguablanca, Spain: Piña et al., 2008; Portneuf-Mauricie Domain, Québec: Sappin et al., 2012; Huangshandong, China: Gao et al., 2013; Manor, 2014). These deposits differ in the size of aerial exposure, the grade and tonnage, and tectonic setting from the Ni-Cu-PGE mineralization typically associated with komatiites, rift-related magmatism, and impact melts. Knowledge derived from these databases, which support the study of the Giant Mascot Ni-Cu-PGE deposit (Manor, 2014), may be used to revise the "orogenic Ni model" and could translate to more efficient exploration practices and guides to future Ni-Cu-PGE exploration in Canada's convergent margin settings (i.e. Cordillera, Appalachians) and similar environments globally.

This study was designed to address the knowledge gaps about the tectonic setting, petrogenesis, age, and generation of Ni-sulphides in the Giant Mascot ultramafic intrusive suite in order to develop exploration criteria for the discovery of deposits formerly classified as "orogenic" (Naldrett, 2011).

Funding and some samples for this study was provided by Natural Resources Canada as part of the Geological Survey of Canada's (GSC) Targeted Geosciences Initiative 4 (TGI-4) program in the Nickel-Copper-Platinum Group Element-Chromium Ore Systems project (Ames and Houlé, 2011) in support of a M.Sc. thesis (first author: Manor, 2014) at the University of British Columbia (Vancouver, B.C.; UBC) under the supervision of Drs. J.S. Scoates (UBC), G.T. Nixon (British Columbia Geological Survey, Victoria, B.C.; BCGS), and D.E. Ames (GSC). This report is a release of multiple databases generated for the Giant Mascot deposit and its geological setting and contains mineral chemistry data, laser ablation ICP-MS analyses, whole rock and trace element geochemical data, modeling calculations, and associated quality control data. These interpretations of the results will be subsequently released in peer-reviewed publications.

INTRODUCTION

The Giant Mascot Ni-Cu-PGE deposit in the Canadian Cordillera remains British Columbia's only past-producing nickel mine (1958–1974), having yielded ~4.2 Mt of ore with an average grade of 0.77% Ni, 0.34% Cu, minor Co, Ag, and Au, and unreported PGE (Christopher and Robinson, 1975). The 'convergent margin' intrusion that hosts the Ni-Cu sulphide ores is a crudely elliptical 3×2 km plug composed of ultramafic cumulate rocks.

This report provides the first systematic documentation of the geochemistry, mineralogy, and textural features of the Ni-Cu-PGE sulphide mineralization and associated platinum-group minerals (PGM) in the Giant Mascot intrusion. New geological mapping (Manor et al., 2014, 2015) provides insight to the mineralogical and textural characteristics of the ultramafic host rocks. Ore formation was deduced utilizing data from epi- and diascopic microscopy, scanning electron microscopy, electron microbeam analyses, whole rock chalcophile and PGE geochemistry, and modeling calculations. This study reveals the complex intrusive history of the ultramafic magma(s) that eventually achieved sulphide saturation and metal enrichment upon emplacement in the crust.

GEOLOGICAL CONTEXT

The Giant Mascot ultramafic intrusion and associated Ni-Cu-PGE deposit lie at the southeastern margin of the Coast Plutonic Complex or Coast Mountains batholith, which extends for more than 1800 km in the Northern Cordillera, from southeastern Alaska to southwestern British Columbia and into the Northern

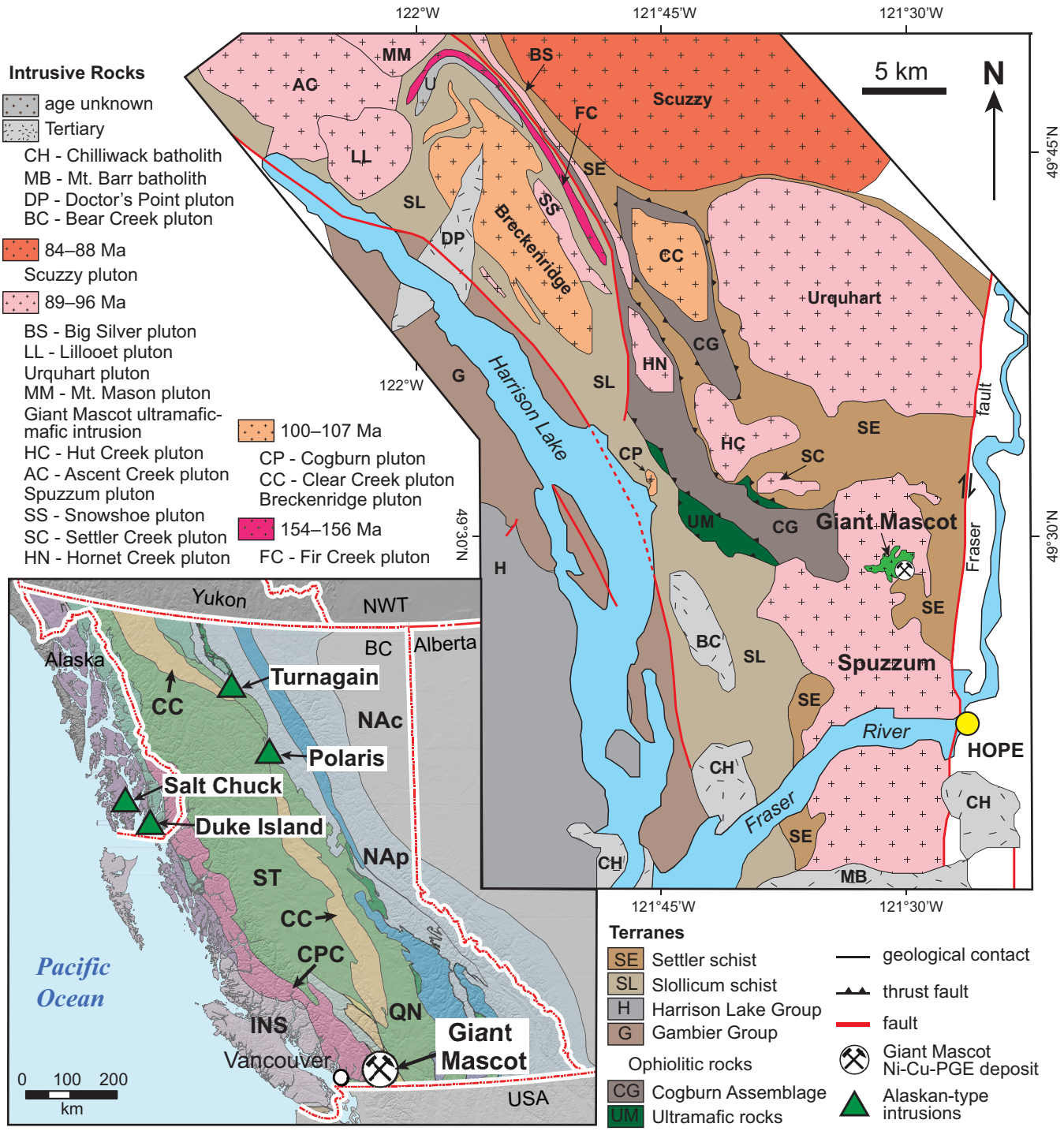

Figure 1. Geology of the Harrison Lake region showing the location of the Giant Mascot ultramafic intrusion and associated Ni-Cu-PGE deposit. The patterns for intrusive rocks indicate Late Cretaceous plutons, which are coloured according to crystallization age (geology modified from Gabites, 1985; Monger, 1989; Brown et al., 2000; and Mitrovic, 2013). The inset (modified after Colpron and Nelson, 2011) shows the location of the Giant Mascot intrusion in southwestern British Columbia relative to Alaskan-type ultramafic intrusions that host Ni-Cu-PGE mineralization.

Cascades in Washington State (Brown and McClelland, 2000; Reiners et al., 2002) (Fig. 1). The study area is located east of Harrison Lake, approximately 12 km north of Hope, British Columbia, and is bounded by Harrison Lake to the west and the Fraser fault to the east (Fig. 1). The Coast Plutonic Complex formed the locus of continental arc magmatism in the Northern Cordillera from the Jurassic to the Paleogene (170–45 Ma; Gehrels et al., 2009). Plutons and batholiths of the southern Coast Plutonic Complex are catazonal to epizonal, tonalitic to gabbroic intrusions that were emplaced in a magmatic arc setting during the

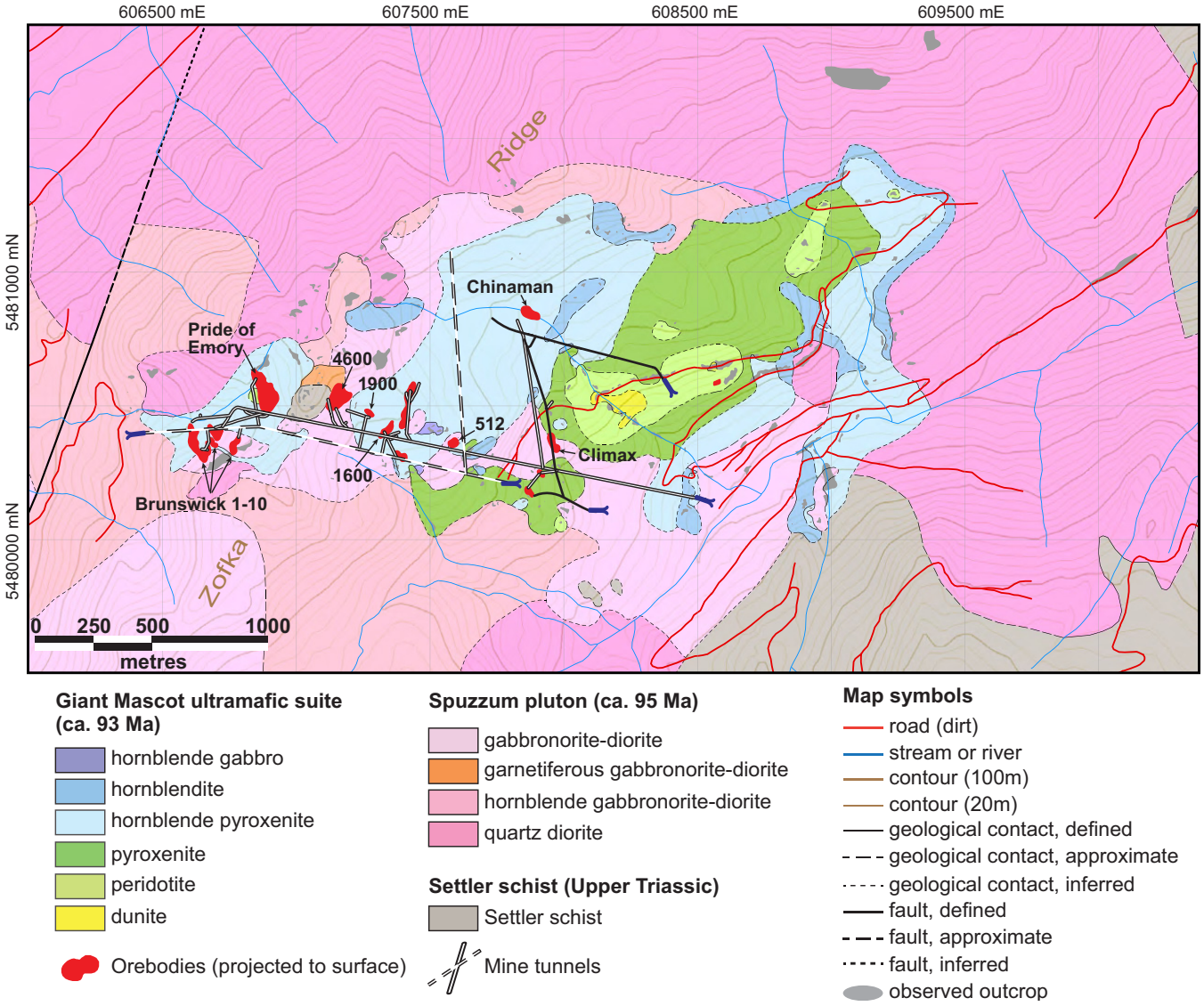

Figure 2. Simplified geological map of the Giant Mascot ultramafic intrusion showing sample locations for U-Pb zircon (Zr) and $^{40}Ar/^{39}Ar$ biotite (Bt), and hornblende (Hbl) geochronology. Sample symbols and colours correspond to those used in all subsequent figures (geology modified from Aho, 1954; Vining, 1977; and Manor et al., 2014). Symbols indicate ultramafic rocks (circles), Spuzzum diorite (orange triangles), Spuzzum pluton quartz diorite (squares), and a mylonite and enclaves (diamonds).

Cretaceous (Fig. 1; 107–76 Ma; Richards, 1971; Brown and McClelland, 2000; Mitrovic, 2013). Metamorphic grade in the Harrison Lake area increases from greenschist in the southwest to amphibolite in the northeast where the Giant Mascot ultramafic suite and northern part of the Spuzzum pluton intruded the upper amphibolite Settler schist (Brown and Walker, 1993).

The rocks that host the Giant Mascot intrusion include the Late Cretaceous Spuzzum pluton and Upper Triassic Settler schist. The Spuzzum pluton is a compositionally zoned dioritic to tonalitic body that intrudes upper amphibolite metapelite of the Settler schist (Pigage, 1973; Richards and McTaggart, 1976; Vining, 1977; Gabites, 1985; Mitrovic, 2013) (Figs. 1 and 2). The Giant Mascot ultramafic intrusion is a small crudely elliptical, 3×2 km body consisting predominantly of dunite, peridotite (lherzolite and harzburgite), pyroxenite (orthopyroxenite, websterite, and olivine websterite), hornblende pyroxenite, and hornblendite (Fig. 2; Aho, 1954, 1956; Manor et al., 2015). The rocks are remarkably fresh and display primary igneous textures involving olivine, orthopyroxene, clinopyroxene, and hornblende, with minor biotite, plagioclase, and accessory rutile, apatite, and zircon. Minor secondary, metamorphic mineralogy varies in intensity and occurs mostly at grain boundaries as tremolite-actinolite, chromian Mg-chlorite, talc, anthophyllite, serpentine, carbonate, and rare zeolite. Ni-Cu-PGE sulphide mineralization is present in 28 steeply plunging pipe-like or lensoid bodies and

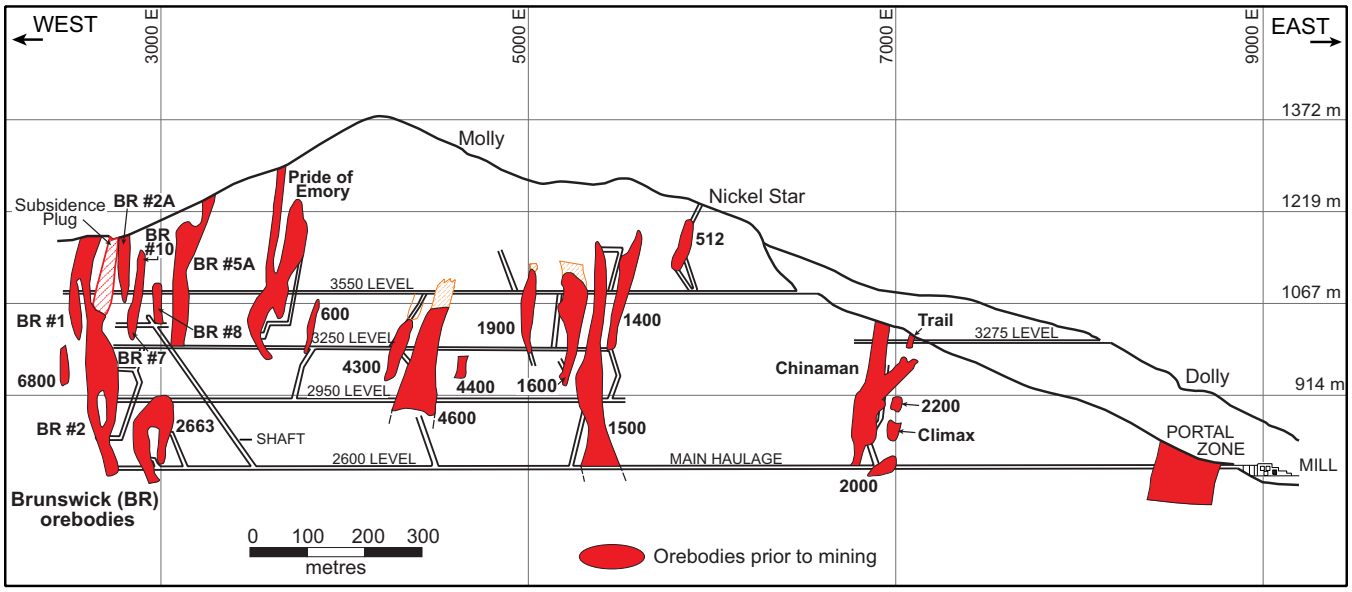

Figure 3. North-looking longitudinal (west-east) section of the entire Giant Mascot deposit. The section extends from the Brunswick orebodies in the northwest to the Portal Zone and mill in the southeast (modified after Clarke, 1969; Christopher and Robinson, 1975). Abbreviation: BR = Brunswick.

also includes several steeply dipping tabular bodies (Christopher and Robinson, 1975; Manor et al., 2015) (Fig. 3).

SAMPLING AND ANALYTICAL TECHNIQUES

Whole-rock lithogeochemistry

A total of 30 samples and four blind duplicates were analyzed for whole rock major element oxide and trace element concentrations at Activation Laboratories, Inc. in Ancaster, Ontario. Results are presented in Figures 4 and 5, and Appendix C. Samples were crushed to 1.7 mm (10 mesh), split to obtain a representative sample, and then crushed again to 106 µm (150 mesh) on Cr-free steel mills. Loss-on-ignition (LOI) for H_2O^+, CO_2, S and other volatiles, was determined from the weight loss after heating at 1050°C for 2 hours. Pulverized material was mixed with lithium metaborate and lithium tetraborate and fused in an induction furnace. The molten melt was immediately poured into a solution of 5% nitric acid containing an internal standard, and was mixed continuously until completely dissolved (~30 minutes). Major element oxide (for Giant Mascot ultramafic-mafic and Spuzzum pluton rocks) and selected trace element concentrations were measured using a Thermo Jarrell-Ash ENVIRO II ICP or a Varian Vista 735 ICP (FUS-MS). Calibration was performed using prepared United States Geological Survey-(USGS) and CANMET-certified reference materials (NIST 694, DNC-1, GBW 07113, W-2a, SY-4, BIR-1a).

A 0.5 g equivalent of the roasted sample was mixed with 6.5 g of a lithium metaborate and lithium tetraborate mixture with lithium bromide (releasing agent) to produce a disk, which was fused in a platinum crucible using an automated crucible fluxer and then poured into platinum molds for casting. Major element (Settler schist rocks) concentrations were measured on a Panalytical Axios Advanced wavelength dispersive X-Ray Fluorescence (XRF) instrument. Matrix effects were minimized by using the heavy absorber fusion technique (Norrish and Hutton, 1969). Titration methods were used to measure FeO concentrations. A cold acid digestion was used with ammonium metavanadate and hydrofluoric acid in an open system. Ferrous ammonium sulphate was added after digestion and potassium dichromate was used as the titrating agent (TITR) (Appendix C).

Select semi-metals were analyzed by aqua regia techniques. A 0.5 g sample was digested in aqua regia at 90°C in a microprocessor-controlled digestion block for 2 hours (AR-MS). A four-acid digestion method was used with a 0.25 g sample, beginning with hydrofluoric acid followed by a mixture of nitric and perchloric acids. Precise heating was used to dry the samples, which were brought back into solution using hydrochloric and nitric acids (TD-MS). Selected samples were fused with sodium peroxide and underwent an acid dissolution (NP-MS). A 30 g sample was mixed with fire assay fluxes (borax, soda ash, silica, litharge) and Ag added as a collector. The mixture was then placed in a fire-clay crucible and subsequently heated in increments to 850°C, 950°C, and 1060°C for 60 minutes. Molten slag was poured from the crucible into a mould to create a lead button. The lead button was then placed in a preheated cupel at 950°C to recover the Ag doré bead, which also contained Au, Pt, and Pd. The Ag doré bead was digested at 95°C in HNO_3 and

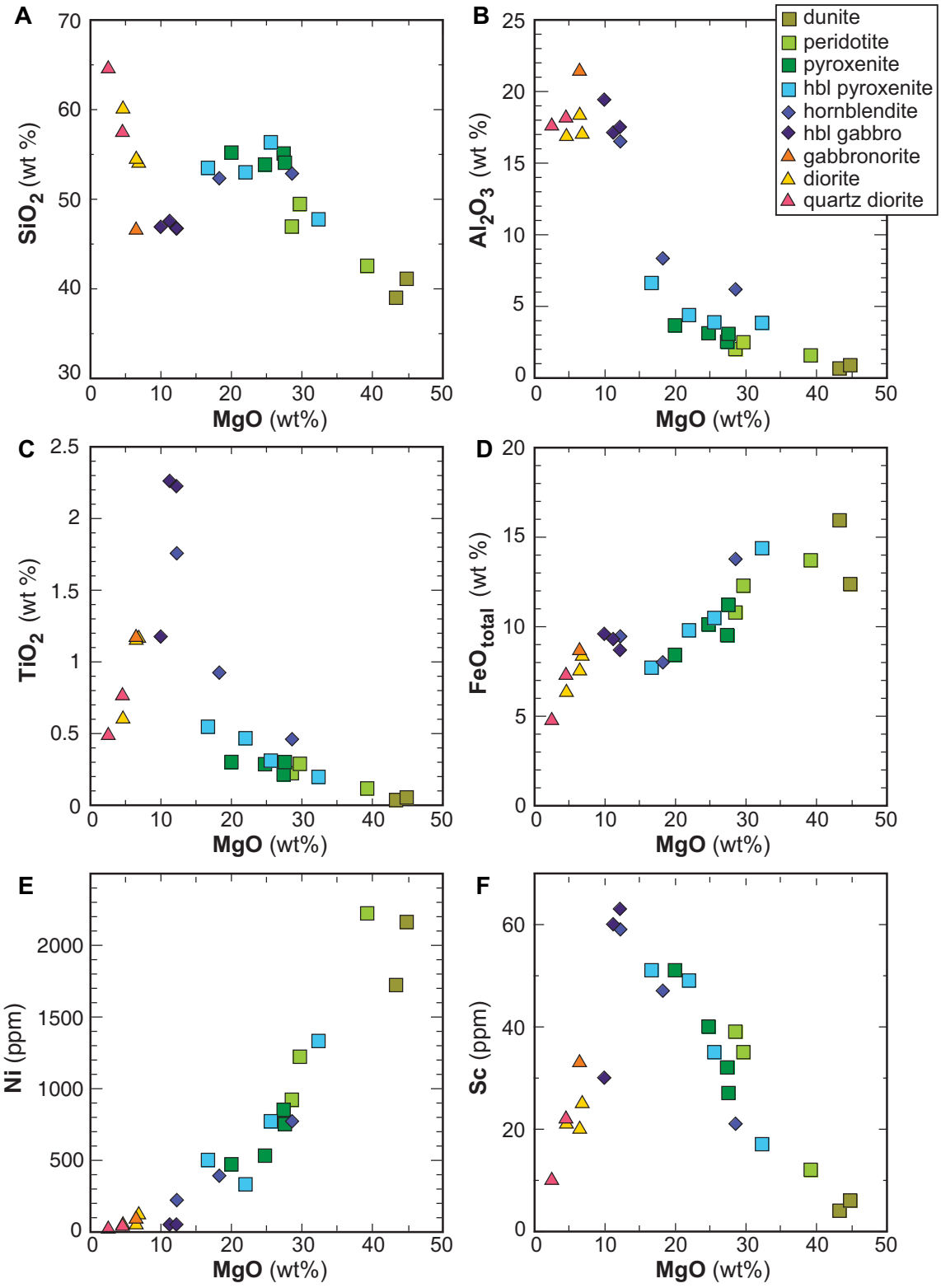

Figure 4. MgO versus select major and trace element variation diagrams for Giant Mascot ultramafic rocks and Spuzzum diorite. **A)** SiO_2 versus MgO; **B)** Al_2O_3 versus MgO; **C)** TiO_2 versus MgO; **D)** FeO_{total} versus MgO; **E)** Ni versus MgO; and **F)** Sc versus MgO. FeOtotal = $FeO+Fe_2O_3$.

HCl with a special complexing agent to prevent the Au, Pd, and Pt from adsorbing onto the test tube. The sample was allowed to cool for 2 hours, after which the sample solution was analyzed for Au, Pt, and Pd (FA-MS). Digested samples from each of the methods outlined above were diluted and selected trace elements were measured using a Perkin Elmer Sciex ELAN 6000, 6100, or 9000 ICP-MS (Appendix C).

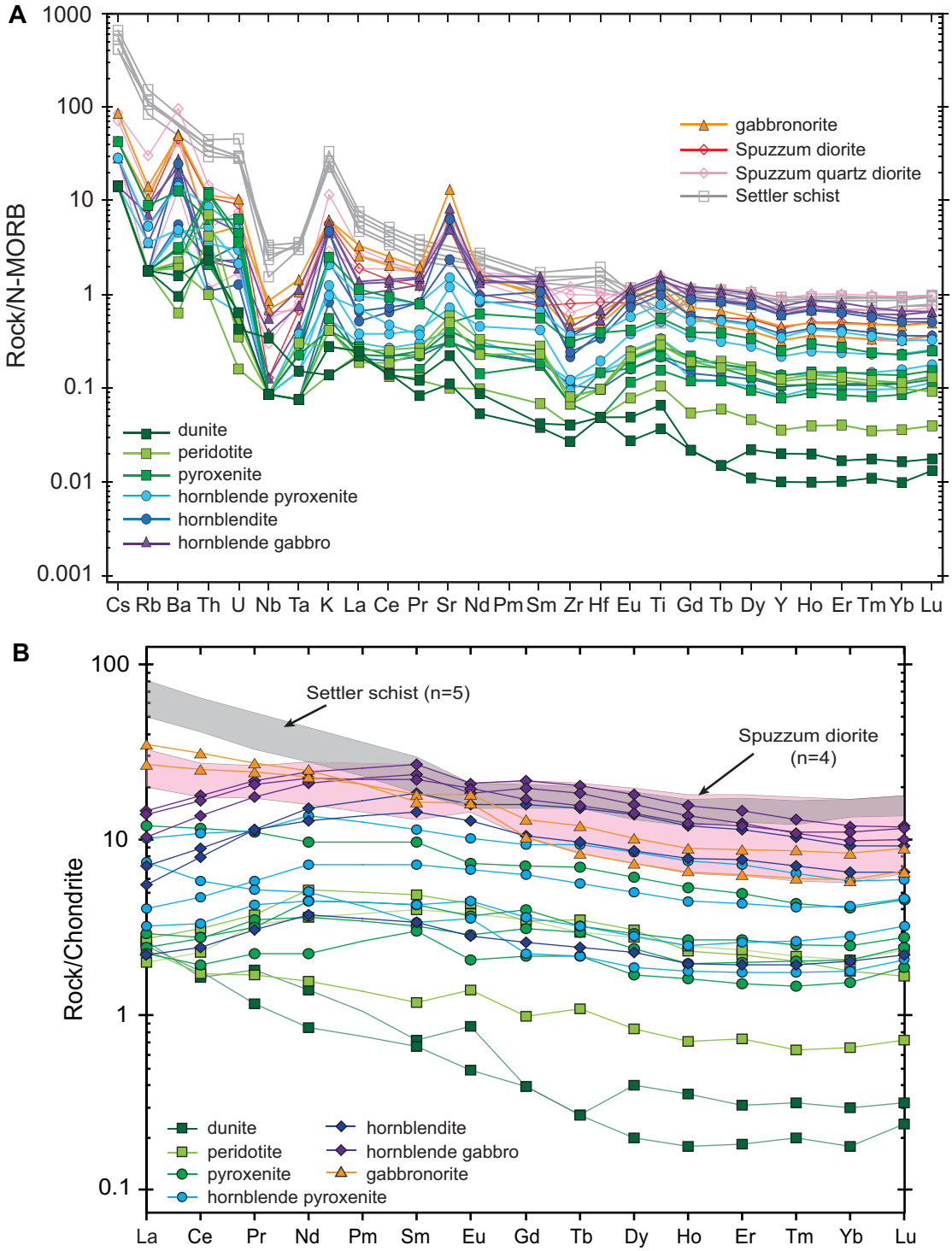

Figure 5. A) N-MORB-normalized trace element concentrations for Giant Mascot ultramafic, Spuzzum pluton, and Settler schist rocks. Solid symbols indicate samples from the Giant Mascot ultramafic intrusion and open symbols represent host rocks. Analyses are normalized to N-MORB values from McDonough and Sun (1995). **B)** Chondrite-normalized rare earth element concentrations for samples in the Giant Mascot ultramafic suite. Host rocks are displayed as a light pink shaded field (Spuzzum diorite) and light grey shaded field (Settler schist). Values are normalized to C1 Chondrite from McDonough and Sun (1995).

Laser ablation ICP-MS analyses of zircon

Following cathodoluminescence imaging of both leached (i.e. chemically abraded) and unleached zircon (Appendix E), grain mounts containing the mineral samples and standards were cleaned with 3N HNO_3 acid prior to analysis to remove any surficial Pb contamination, a step that removes the necessity for pre-ablating the samples. Laser ablation, mass spectrometry, and data quantification and processing of samples were completed at Pacific Centre for Isotropic and

Table 1. LA-ICP-MS instrumentation, operating conditions, and quantification.

Laser Ablation (LA) sampler	
Model	Resonetics RESOlution M-50-LR Class I
Wavelength	193 nm (Coherent COMPex Pro 110 UV excimer laser source)
Pulse duration (FWHM)	4 ns
Sample cell	Laurin 2-volume cell, each with separate carrier gas-in port
Gas flows:	
1) He carrier into cup	0.53 L/min
2) He carrier into cell base	0.53 L/min
3) Ar make up	0.53 L/min
ICP-MS	
Model	Agilent 7700x quadrupole with additional interface rotary pump
Shield torch	Used
RF power	1350 W
Sampling depth	30–40 μm
ThO^+/Th^+	<0.2%
U/Th sensitivity ratio (NIST612)	1.01–1.05
Data acquisition parameters - spot analysis	
Laser spot	Round, 17 μm nominal diameter (33 μm for 03GNX-3-1-1 and 11GNX-1-3-1)
Laser energy density at sample	5 J/cm2
Laser repetition rate	5 Hz
Isotopes determined (dwell in ms)	^{29}Si, ^{43}Ca, ^{49}Ti, ^{85}Rb, ^{88}Sr, ^{89}Y, ^{90}Zr, ^{93}Nb, ^{139}La, ^{140}Ce, ^{141}Pr, Nd (^{143}Nd, ^{146}Nd), ^{147}Sm, ^{153}Eu, ^{163}Dy, ^{165}Ho, ^{166}166Er, ^{169}Tm, ^{172}Yb, ^{175}Lu, ^{177}Hf, ^{181}Ta, ^{202}Hg, Pb (^{204}Pb, ^{206}Pb, ^{207}Pb, ^{208}Pb), ^{232}Th, and U (^{235}U, ^{238}U)
Mass sweep time	705 ms
Analysis time	100 s: ~60 s gas blank, up to ~60 s of ablation
Quantification	
Calibration standards	
1) U-Pb geochronology	Plešovice (Sláma et al., 2008) and Temora2 zircon (Black et al., 2004)
2) Trace elements	NIST612 glass
Data processing	Igor ProTM Iolite extension (Paton et al., 2011)

Geochemical Research (PCIGR) (Table 1). The laser was imaged onto the sample using different apertures allowing for a spot size between 5 and 350 μm. To maximize stability, the entire laser path was treated with a N_2 flux. This sample chamber facilitated the investigation of several samples within one analytical session and/or larger specimen, and also assured high sensitivity, low fractionation, and short washout times. Ablation was carried out in a cell with a volume of about 20 cm^3, and a He gas stream that ensured good signal stability and low U-Pb fractionation (e.g. Eggins et al., 1998). Standards were analyzed throughout the sequence, two for every five unknowns, to correct for drift and to characterize down-hole fractionation for U-Pb isotopic ratios. Laser ablation instrumentation, operating conditions, and quantification are summarized in Table 1. Trace element concentrations and age dates are listed in Appendix E.

Chalcophile, platinum-group element, and sulphur analyses

Platinum group element (Ir, Ru, Rh, Pt, Pd, Au) and chalcophile element (Ni, Cu, Co) concentrations of 39 whole rock samples and 3 duplicates were measured using nickel-sulphide fire-assay (NiS-FA) ICP-MS and atomic absorption spectroscopy techniques, respectively, at Geoscience Laboratories (Geolabs) in Sudbury, Ontario. Samples were crushed to 74 μm (200 mesh) using a high-chrome steel mill to avoid contamination of precious metals.

Nickel sulphide fire-assay techniques at Geolabs have been documented by Richardson and Burnham (2002), and follow procedures outlined in Shazali et al. (1987) and Jackson et al. (1990). Nickel, sulphur, sodium carbonate, and sodium tetraborate were added to a 15 g aliquot of sample powder, and fused for 1.5 hours in a fire-clay crucible at 1050°C. Following cooling, the crucible was broken to recover a nickel sulphide button. This button was dissolved with HCl in a closed Teflon™ vessel to remove any NiS matrix. The co-precipitation of the NiS button with tellurium produced a concentrate containing all the Au and PGEs that had been lost during button dissolution. Concentrates were then vacuum-filtered, re-dissolved

in aqua regia, and brought to volume with deionized water prior to analysis by a Perkin-Elmer ELAN 5000 inductively coupled plasma mass spectrometer (ICP-MS). Osmium was not reported due to the potential loss as a volatile oxide during the aqua regia re-dissolution stage. Reference materials used were CANMET-certified TDB-1, WPR-1, WGB-1, and WMG-1, and an in-house komatiite sample OKUM.

The remaining <74 μm pulps from the same crush as the NiS-FA method were mixed with a three-acid (hydrofluoric, nitric, and perchloric) mix in an open Teflon™ digestion vessel and heated until dry. A solution was produced by adding a second acid mixture, which was transferred to a 50 mL volumetric container and diluted with 10% HNO_3 respective to the volume of sample. Chalcophile element (Ni, Cu, Co, Cd, Zn, Li, Pb) concentrations were measured by atomic absorption methods with a Varian Atomic Absorption Spectrometer AA280FS Series.

Sulphur and carbon measurement techniques have been outlined in Amirault and Burnham (2013). Sample material was taken from a 0.2 g pre-measured aliquot and combusted from radio-frequency inductive heating with a constant stream of purified oxygen. Gases (CO_2 and SO_2) were produced and detected by non-dispersive infrared (NDIR) cells. Concentrations were then measured by a LECO CS844 carbon and sulphur analyzer. Results for all analyses are reported in Appendix H.

Electron microprobe analyses

Nickel concentrations in olivine were determined using polished petrographic thin sections (n=15) that had been carbon coated and prepared in the Electron Microbeam/X-Ray Diffraction Facility at UBC, Vancouver. For each sample, five olivine grains were selected for analysis and core-mid-rim transects were probed with a fully automated Cameca SX-50 scanning electron microprobe with four vertical wavelength-dispersion X-ray (WDX) spectrometers and a fully integrated SAMx energy-dispersion X-ray (EDX) spectrometer. Major elements in olivine were analyzed using a 15 keV accelerating voltage, 20 nA beam current, 10 μm diameter beam, 30 s peak count time, and 10 s background count time. Second analyses on identical spots yielded more precise Ni and Ca concentrations at a 15 keV accelerating voltage, 100 nA beam current, 10 μm diameter beam, 100 s peak count time, and 10 s background count time. Natural and synthetic standards were used for calibration and procedural set-up of the instrument prior to each day of analysis. Data were reduced by the "PAP" $\Phi(\rho Z)$ procedure of (Pouchou and Pichoir, 1991). All analyses are reported in Appendix D.

Quantitative mineral analyses of sulphides and platinum group minerals were determined on carbon-coated, polished petrographic thin sections (n=9) using an automated four-spectrometer Cameca Camebax MBX electron microprobe by wavelength-dispersive X-ray analysis at the Department of Earth Sciences, Carleton University, Ottawa. Raw X-ray data were converted to elemental weight percent by the Cameca PAP matrix correction program. Telluride and precious-metal minerals were analyzed using a 20 keV accelerating voltage, 35 nA beam current, 2 μm diameter beam, and a counting time of 10 s or 40,000 accumulated counts.

RESULTS

The Giant Mascot ultramafic intrusion and country rocks

Major and trace element geochemistry

Major and trace element abundances of the Giant Mascot ultramafic suite and Spuzzum pluton host rocks are reported in Appendix C and illustrated in Figures 4 and 5. The ultramafic cumulates (dunite, peridotite, pyroxenite, hornblende pyroxenite, and hornblendite) are characterized by 38.2–54.1 wt% SiO_2 and 11.7–43.4 wt% MgO and mafic rocks (hornblende gabbro and gabbronorite) by 44.5–53.6 wt% SiO_2 and 6.3–11.6 wt% MgO, whereas diorite of the Spuzzum pluton contains 45.7–63.4 wt% SiO_2 and 2.4–6.3 wt% MgO (Fig. 4). Additional variations in Al_2O_3, TiO_2, FeO_{total}, Ni, and Sc clearly define the ultramafic suite from Spuzzum diorite (Fig. 4).

Trace element abundances from whole rock samples of the Giant Mascot ultramafic-mafic intrusion span several orders of magnitude above and below normal mid-ocean ridge basalt (N-MORB) in the primitive mantle-normalized trace element diagram (Fig. 5A). Large ion lithophile element (LILE: Cs, Rb, Ba, K, Sr, U) abundances are elevated relative to high field strength elements (HFSE: Nb, Ta) and yield high LILE/HFSE ratios, which are characteristic of typical arc magmas (e.g. Pearce et al., 1995). The whole rock samples are slightly enriched in rare earth elements (REEs) relative to chondrite, and have relatively flat patterns from light to heavy REE (LREE and HREE, respectively) contents (Fig. 5B).

Gabbroic rocks have the highest trace element concentrations, the most pronounced positive Sr anomaly (1200 ppm), and the steepest chondrite-normalized REE pattern ($[La/Yb]_N$=2.4–6.0; Fig. 5B). Analytical results of hornblende-bearing rocks (i.e. hornblendite and hornblende gabbro) are similar to those of gabbro, but have slightly lower total trace element concentrations; hornblende gabbro contains the highest HREE values. The samples from both rock types have con-

cave-down REE patterns that yield $[La/Yb]_N$ values of 0.60 to 1.3, which is analogous to REE patterns of granodiorite (e.g. Gromet and Silver, 1983; Fig. 5B). Comparatively, data from olivine-bearing cumulate rocks (i.e. peridotite, and pyroxenite) show the lowest trace element abundances with the flattest REE patterns ($[La/Yb]_N$=1.0–3.0; Fig. 5). Analytical results for most trace elements in dunite are less reliable due to values that are near detection limits.

The trace element patterns for hornblendite, hornblende gabbro, and gabbro from Giant Mascot are similar to those for Spuzzum diorites, an exception being a small positive Zr anomaly in the quartz diorite (Fig. 5A). Settler schist samples display the highest LILE and HFSE concentrations relative to Giant Mascot and Spuzzum samples, including a pronounced negative Ti anomaly, $[La/Yb]_N$ values of 3.2 to 4.8, and highest LREE values (Fig. 5B).

Olivine compositions

The forsterite (Fo) contents in olivine from 220 analyses of barren and mineralized rocks of the Giant Mascot ultramafic intrusion range from $Fo_{80.6}$ to $Fo_{89.11}$ (Appendix D). A dunite containing disseminated sulphides (sample 12MMA-7-8-1) has the most restricted range of forsterite content ($Fo_{83.7–84.8}$). Mineralized and barren peridotite yield similar olivine compositions of $Fo_{83.0–89.1}$ and $Fo_{82.5–88.1}$, respectively. Pyroxenite with sulphide mineralization has the largest range of olivine compositions ($Fo_{80.6–88.2}$), and barren pyroxenite is restricted to $Fo_{82.1–83.8}$. Forsterite content of olivine cores and rims can vary as much as ~2.5 mol%, and rims are typically more Mg-rich than cores in mineralized samples. Barren rocks have more homogenous olivine compositions, with relatively smaller compositional variation ($Fo_{87.4–88.1}$ and $Fo_{82.1–85.0}$) and more Fe-rich rims.

The nickel concentrations in olivine in the Giant Mascot rocks are highly variable, from 336 to 3859 ppm, with anomalously high nickel contents (>2000 ppm) occurring in the range of $Fo_{80.6}$ to $Fo_{87.4}$ (Appendix D2). In dunite, Ni concentrations in olivine range from 731 to 1464 ppm. Mineralized peridotite and pyroxenite have the highest and most variable Ni concentrations (336–3859 ppm and 336–3439 ppm, respectively) and barren peridotite (576–1797 ppm) and pyroxenite (666–1018 ppm) have the lowest.

Ti-in-zircon thermometry

Minimum crystallization temperatures of zircon (hereafter T_{zrn}) in the ultramafic rocks were calculated using the Ti-in-zircon thermometry method of Ferry and Watson (2007) and are described in detail in Manor (2014). The calculated T_{zrn} values for two pyroxenite grains range from 646 to 799°C, with averages of 696 ±68°C (sample 12MMA-5-4-1, n=9) and 720 ±44°C (sample 03GNX-3-1-1, n=27) (Appendix E4). Zircon from a hornblende pyroxenite (sample 12MMA-2-4-1) has a lower T_{zrn} of 601 to 682°C and an average of 640 ±72°C (n=9); zircon in a hornblendite (sample 13MMA-2-7-1) gives a wide range of T_{zrn} of 662 to 837°C, averaging 762 ±58°C (n=24). The relatively higher T_{zrn} and larger errors recorded from zircon in the hornblendite are likely the result of the microporous and altered grains. The calculated T_{zrn} for a Spuzzum diorite (sample 12MMA-2-3-1) ranged from 681 to 816°C, with an average of 741 ±62°C (n=16). Zircon from three Spuzzum quartz diorite samples (11GNX-1-3-1, 12MMA-2-1-5, and 12MMA-6-5-1) indicate a wide range of T_{zrn}, from 658 to 844°C and a similar average of 741 ±49°C (n=43). The overall average crystallization temperature for zircon in the Giant Mascot intrusion is slightly lower (~710°C) than in the Spuzzum pluton (~740°C), although both temperatures are identical within error. A full record of laser ablation ICP-MS spot locations and trace element analyses for zircon from both rock suites can be found in Appendices E2 and E3.

The Giant Mascot Ni-Cu-PGE deposit

Sulphide and platinum group element geochemistry

A total of 44 mineralized whole rock samples from 11 Giant Mascot orebodies were analyzed for S and Ni-Cu-Co contents, and platinum group element (PGE: Ir, Ru, Rh, Pd, Pt) and Au concentrations (Table 2; Appendix H). Whole rock sulphur contents range from 0.97 to 33 wt% and are directly proportional to the modal abundance of sulphide, and have relatively little association with rock type. Analyses of mineralized olivine-rich rocks (e.g. dunite, peridotite) have elevated Ni, Cu, Pd, and Pt concentrations (averages: 1.8 wt% Ni, 0.7 wt% Cu, 239 ppm Pd, 124 ppm Pt). They are also characterized by Ni contents above that of stoichiometric pentlandite, reflecting another mineralogical host for nickel (e.g. olivine).

Variations in chalcophile element contents are a function of mineralization type: net-textured ores have the lowest Ni, Cu, and PGE contents and the semi-massive, massive, and disseminated ores are richest. Disseminated sulphides have low S (0.97–12.8 wt%), high Ni and PGE, and low Cu (average Ni/Cu=3.6, $Cu/Pd=2.3\times10^4$). In net-textured sulphides, there is a wider range of S content (2.3–32 wt%), relatively higher Ni, elevated Cu (Ni/Cu=2.9), and lower PGE ($Cu/Pd=1.5\times10^5$). The semi-massive sulphides have a more restricted range of S content (13–19 wt%), Ni/Cu ratios of 1.9, and moderate PGE values ($Cu/Pd=3.5\times10^4$). For massive sulphides, the results yield the highest S and average Ni contents (22–

Table 2. Whole rock chalcophile and platinum group element analyses for sulphide-rich rocks from the Giant Mascot Ni-Cu-PGE deposit.

			wt%	ppm			ppb					
Sample	**Rock type[1]**	**Texture[2]**	**S**	**Ni**	**Cu**	**Co**	**Ir**	**Ru**	**Rh**	**Pt**	**Pd**	**Au**
1600 orebody												
179-E-847	dunite	SM	15.7	30973	13609	346	272	378	182	170	768	8.63
179-E-410	peridotite	D	11.6	44145	1303	715	136	196	142	323	824	7.42
1900 orebody												
179-E-364	ol pyroxenite	D	5.39	12541	4020	358	12.3	13.9	14.5	14	136	42.2
179-E-367	hbl opxite	NT	2.31	4061	4104	167	4.13	5.44	4.44	19.6	59.8	49.5
4600 orebody												
M29-30	hbl opxite	D	0.97	2560	2962	102	1.42	1.91	1.26	101	49	37.4
3050 Crosscut												
EI-71-621*	pyroxenite	D	4.56	11000	3600	280	7.5	bdl	15	150	150	61
EI-71-622*	pyroxenite	M	3.42	6000	4600	230	3.6	25	4	46	51	11
EI-71-659A	hbl pyroxenite	M	28.87	39748	1891	2717	50.3	66.4	44.2	81.2	178	4.2
EI-71-659*	hbl pyroxenite	M	21.9	23000	6700	1300	21	28	24	bdl	150	5
EI-71-659B	hbl pyroxenite	M	30.2	32000	16000	2000	19	50	16	31	93	6
EI-71-624	hblite dyke	vein	10.1	32000	2200	570	51	59	100	89	630	33
Pride of Emory												
13MMA-9-6-1A	peridotite	SM	12.82	393	1773	804	6.59	7.37	6.82	5.49	150	2.6
13MMA-9-6-1B	peridotite	SM	12.55	13036	4013	599	6.97	7.59	6.52	71.1	146	12.2
13MMA-9-6-4	peridotite	NT	7.48	9007	3420	367	4.42	3.42	6.32	16.3	55.7	13.9
11AV-200	pyroxenite	NT	12.03	23097	5191	711	2.56	1.35	8.69	8.34	137	7.6
11AV-201	pyroxenite	D	8.94	19591	5965	530	2.06	0.97	5.54	115	198	26.4
11AV-202a	pyroxenite	NT	9.61	12942	3837	754	1.08	1.2	2.14	3.63	20	2.66
11AV-204	pyroxenite	NT	11.79	27587	3695	870	12	13.7	10.4	12.2	289	3.74
179-E-763	pyroxenite	NT	11	11989	6757	489	4.34	6.26	1.18	2.53	13.6	4.29
179-E-345	opxite	NT	10.1	13104	1009	590	0.32	0.42	0.81	0.87	18.2	3.04
Brunswick orebodies												
179-E-2	dunite	D	5.83	15926	12747	440	3.76	4.6	3.36	16.2	66.8	15.2
179-E-839	ol pyroxenite	NT	16.6	16583	13759	812	3.33	5.66	2.53	25.5	37.9	6.33
179-E-765	pyroxenite		14.7	16835	2104	709	6.55	9.95	3.01	0.71	49.5	2.91
179-E-838	opxite	NT	17.7	19263	24937	793	7.35	11.4	4.39	58.5	77.4	7.56
Chinaman												
EI-71-623	pyroxenite	D	10.5	31000	4500	530	70	46	100	500	820	73
Climax												
EI-71-615	pyroxenite	D	3.55	9100	5600	190	5.3	23	8	470	730	81
3550 East Portal dump												
RHP01-075	peridotite	SM	19.1	20514	7288	978	7.81	13.6	5.32	6.99	49.3	9.98
RHP01-152	peridotite	NT	32.6	84034	47696	2027	508	644	369	1511	2018	25.6
12MMA-5-8-1	pyroxenite	NT	14.31	13577	7239	614	5.47	8.17	4.26	0.66	40.8	20.1
12MMA-5-8-2	pyroxenite	NT	10.5	8890	10053	587	0.66	1.01	0.56	16.3	25.5	6.93
12MMA-5-8-4	pyroxenite	NT	19.97	20249	5971	1027	7.61	12.8	5.45	65.7	59.7	13.2
12MMA-5-8-6	pyroxenite	NT	14.9	26425	4680	729	0.65	0.48	2.34	53	170	28
RHP01-077	pyroxenite	D	7.05	14124	2439	422	7.53	9.29	6.59	3.84	94.2	6.46
RHP01-151	pyroxenite	D	6.29	8676	1056	311	2.33	3.59	1.7	4.02	25.4	5.23
12MMA-5-8-3	hbl pyroxenite	NT	7.43	6752	1362	497	0.51	0.81	0.5	0.33	16.9	13.9
12MMA-5-8-5	hbl pyroxenite	D	2.37	7446	2515	201	14.1	20	11.8	253	186	49
Dolly Adit dump												
12MMA-7-10-2	pyroxenite	NT	12.76	19990	5895	741	23	25.6	27.6	245	226	25.9
12MMA-7-10-3	pyroxenite	NT	14.09	27872	14944	979	8.31	7.3	14.9	123	420	19
12MMA-7-10-4	pyroxenite	D	6.87	11124	4409	420	17.3	20.4	16.4	14.1	107	3.78
12MMA-7-10-5	pyroxenite	D	12.78	21584	2411	930	8.47	8.66	11.9	2.19	323	1.36
12MMA-7-10-6	pyroxenite	D	3.71	9126	2393	301	3.35	3.75	4.33	61.5	88.5	20.2
12MMA-7-10-7	pyroxenite	D	1.22	1548	5934	88	0.34	0.32	0.6	104	318	111
Pride of Emory dump												
RHP01-088	pyroxenite	SM	8.45	14128	16133	518	8.51	4.21	26.2	12.7	193	4.5

*Analyses from Hulbert (2001); bdl = below lower limit of detection.

[1] hbl = hornblende, hblite = hornblendite, ol = olivine, opxite = orthopyroxenite.

[2] Mineralization texture of sulphide minerals in whole rock; D = disseminated, M = massive, NT = net-textured, SM = semi-massive.

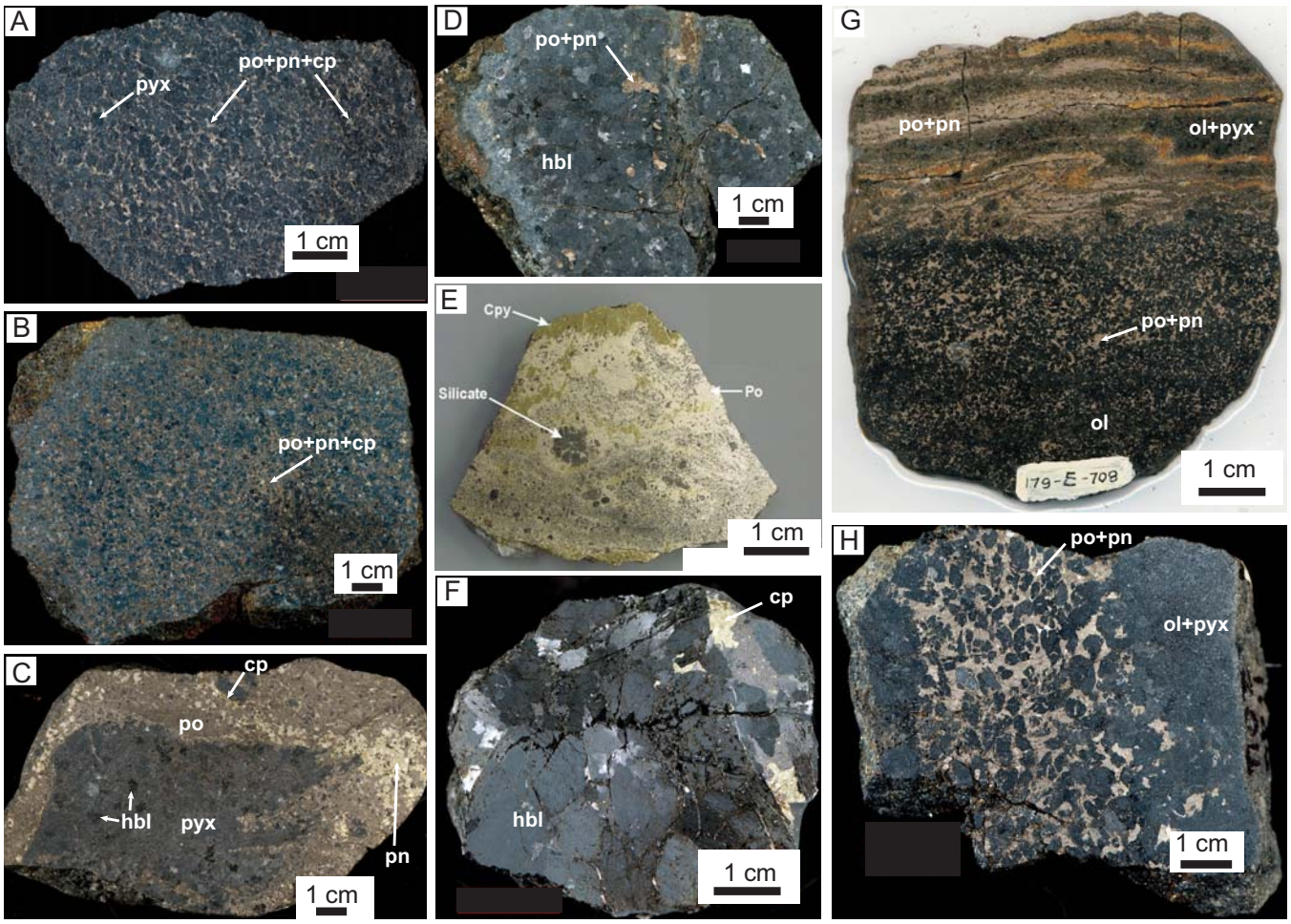

Figure 6. Principal ore types in the mineralization of the Giant Mascot intrusive suite. **A)** Moderately net-textured pyrrhotite, pentlandite, and chalcopyrite in pyroxenite (sample 11AV-201). **B)** Weakly net-textured pyrrhotite, pentlandite, and chalcopyrite in pyroxenite (sample 11AV-200). **C)** Massive pyrrhotite, pentlandite, and minor chalcopyrite in hornblende pyroxenite (sample 71-EI-659). **D)** Disseminated pyrrhotite and pentlandite within hornblendite (sample 71-EI-622). **E)** Massive pyrrhotite containing chalcopyrite veins and a rounded silicate inclusion (photo by R.H. Pinsent) (sample RHP01-076). **F)** Hornblendite with chalcopyrite veins (sample 71-EI-624). **G)** Folded layers of disseminated pyrrhotite, pentlandite, and olivine-rich peridotite at a contact with dunite (sample 179-E-709; Aho, 1954). **H)** Strongly net-textured pyrrhotite and pentlandite in peridotite (sample 11AV-204). Mineral abbreviations: cp = chalcopyrite; hbl = hornblende; ol = olivine; pn = pentlandite; po = pyrrhotite; pyx = pyroxene.

30 wt% and <2.5 wt%, respectively), and Ni/Cu and Cu/Pd ratios are similar to those of semi-massive sulphides (2.3 and 4.8×10^4, respectively).

Procedure for calculating 100% sulphide from whole-rock Ni, Cu, and PGE analyses

Corrections for metal contents in 100% sulphide (i.e. tenor) were calculated for 39 samples from this study and 12 samples from Hulbert (2001), including 8 samples from McLeod (1975) and 4 samples from Eckstrand (1971, GSC sample collection) (Appendix I). The correction parameters from Naldrett et al. (2000) were used for Ni, Cu, Co, S, Ir, Ru, Rh, Pt, Pd, and Au: a method that utilizes the presence of significant Ni contents in olivine to correct for the Ni tenor in sulphide. Kerr (2003) used a simpler approach that accounted for generalized 'nonsulphide Ni' to explain any Ni not included in the true tenor. The measured elemental concentrations were first converted to atomic proportions to determine the amount of S in pyrrhotite, pentlandite, and chalcopyrite; the S remaining from the calculation was assigned to pyrrhotite. Based on normalized sulphide proportions, the amount of S and Fe applied to pyrrhotite, pentlandite, and chalcopyrite in massive sulphide were determined by multiplying by the ideal stoichiometric S wt% (36.5, 33.3, and 34.9 wt%, respectively) and Fe wt% (63.5, 36.2, and 30.4 wt%, respectively) in each of the three minerals. Proportions of sulphide were then determined based on the computed S in massive sulphide; Fe associated with sulphide was iterated based on this sulphide proportion. The total S in massive sulphide relative to the original S assay was used as a conversion factor to determine the raw sulphide metal contents (i.e. tenor). Platinum group elements were calculated with the same conversion factor, assuming that the PGE origi-

Table 3. Modal abundances of minerals in sulphide-rich rocks from the Giant Mascot Ni-Cu-PGE deposit.

Sample	Ore texture[1]	Rock type[2]	Location[3]	Mineralogy[4] (vol. %)								
				Plag	Ol	Opx	Cpx	Hbl	Act	Cum	Phl	Tlc	Srp
71-EI-615A*	NT	Pyroxenite	Climax			15	35	10					
71-EI-624A*	V	Hornblendite	3050 Crosscut					80				tr	
71-EI-632*	D	Orthopyroxenite	DDH-U-3841	1	tr	75		10					
71-EI-634	D	Orthopyroxenite	DDH-U-3841	4	tr	75		10					
71-EI-635*	NT	Hbl peridotite	DDH-U-3841		45	8	3	10			tr		
71-EI-636	NT	Orthopyroxenite	DDH-U-3841		tr	66		5					
71-EI-639B*	NT	Hbl orthopyroxene	DDH-U-3841			70		15					
71-EI-657*	NT	Pyroxenite	DDH-U-3869			34	4	3					
71-EI-659A*	M	Hbl pyroxenite	3050 Adit		tr	20	24	30					
71-EI-659B*	B	Hbl pyroxenite	3051 Adit			30	34	35					
11AV-200*	NT	Ol orthopyroxenite	Pride of Emory		15	51		5	2				
11AV-201*	D	Dunite	Pride of Emory		65	5		4	tr				
11AV-202	D	Hbl harzburgite	Pride of Emory		25	27		8	tr				
11AV-204	NT	Hbl peridotite	Pride of Emory		48		12	tr					
179-E-410*	D	Hbl peridotite	1600 orebody		40	5		25			4		3
179-E-847*	SM	Hbl peridotite	1600 orebody		25	5		20					5
RHP01-078*	NT	Hbl peridotite	3550 East Portal dump		15	15		40					7
RHP01-109*[5]	D	Hbl pyroxenite	Mill site dump	4		45		40	5	1	4		
RHP01-118	NT	Ol pyroxenite	Dolly Adit dump		6	18	20	18					
RHP01-152*	NT	Harzburgite	3550 East Portal dump		27	28		1					
SVA-75.8-14.5*	D	Hbl pyroxenite	Climax			38	4	55					
M29-21*	SM	Peridotite	4600 orebody		25	25	4	2	tr				
12MMA-5-8-1	NT	Pyroxenite	3550 East Portal dump	5		55		10	tr				
12MMA-5-8-2	NT	Pyroxenite	3550 East Portal dump			75		5					
12MMA-5-8-3*	INT	Pyroxenite	3550 East Portal dump			78		6					
12MMA-5-8-4	NT	Orthopyroxenite	3550 East Portal dump	2	tr	65		5					
12MMA-5-8-5A*[5]	D	Hbl peridotite	3550 East Portal dump		40	5		30	3		2		

Sample	Mineralogy[4] (vol. %)																		
	Chl	Carb	Apa	Rut	Ilm	Mt	Chr	Po	Troi	Pn	Cp	Cub	Py	Mc	Mk	Ag-pn	Sph	Total sulphide	PGM
71-EI-615A*								22		13	1		3					39	tr
71-EI-624A*		tr				3		tr		tr	15		tr			tr	tr	15	
71-EI-632*						tr	tr	5		2	4		tr		tr	tr		11	tr
71-EI-634		tr					tr	2		5	4		tr			tr		11	
71-EI-635*						2	tr	20		7	2		2					31	
71-EI-636		tr					tr	10		4	9		4	tr				27	
71-EI-639B*							tr	2		2	10		tr			tr		14	
71-EI-657*		tr						45		14	tr		1					60	tr
71-EI-659A*	tr	tr		tr		tr		18		4	2		2					26	
71-EI-659B*	tr	tr				tr		tr		tr	tr							tr	
11AV-200*	tr				tr	tr	tr	16		8	1		1					26	
11AV-201*	tr					1	tr	12		7	5		tr					24	
11AV-202	tr	tr				tr	tr	22		11	6							39	
11AV-204	tr	tr						22		11	6							39	
179-E-410 *			tr				tr	15		7	tr		1	tr				23	tr
179-E-847*	1					tr	tr	24		13	7		1	tr				45	tr
RHP01-078*	1					tr	tr	2		2	20	tr	1	tr	tr			25	tr
RHP01-109*[5]		tr	tr	tr	tr				1	tr	tr	tr						1	
RHP01-118						tr	tr	20		10	10		tr					40	
RHP01-152*	tr				tr	tr	tr	5		13	16		6	tr	tr			40	tr
SVA-75.8-14.5*	tr	tr				tr	tr	1		tr	1		0.5					2	
M29-21*	tr	tr				tr	tr	20		10	12		1					43	tr
12MMA-5-8-1		tr		tr			4	15		7	3							25	
12MMA-5-8-2	tr			tr			tr	12		5	3							20	
12MMA-5-8-3*	tr	tr		tr			tr	4		1	tr							5	
12MMA-5-8-4		tr		tr			tr	16		4	4							24	
12MMA-5-8-5A*[5]	tr	tr				tr	tr	tr	8	6	4	1		tr	tr		tr	19	

*EMPA sample for sulphide and PGM compositions.

[1]B=barren, D=disseminated sulphide, INT=interstial sulphide, M=massive sulphide, NT=net-textured sulphide, SM=semi-massive sulphide, V=vein.

[2]DDH-U-3841 is oriented down-plunge from the Chinaman orebody.

[3]Hbl=hornblende; Ol=olivine.

[4]Ag-pn=argentopentlandite, Chr=chromite, Cp=chalcopyrite, Cub=cubanite, Ilm=ilmenite, Mc=marcasite, Mk=mackinawite, Mt=magnetite, PGM=platinum group minerals, Pn=pentlandite, Po=pyrrhotite, Py=pyrite, Sph=sphalerite, Troi=troilite, tr=trace.

[5]troilite:pyrrhotite=1:1.

Table 4. Mineralogy of Ni-Cu-PGE sulphides, Giant Mascot deposit.†

Mineral[1]	Formula	Description[2]	Photo evidence
Major ore minerals			
pyrrhotite	$Fe_{1-x}S$	most abundant sulphide, po:pn = 2:1; massive or veins in fractures in silicates	Figs. 6, 7A-F, J-L, 10A, B, D, E, H, K
pentlandite	$(Fe,Ni)_9S_8$	dominant Ni-ore mineral; massive and blocky or exsolution lamellae in po, tro, Ag-pn	Figs. 6, 7A-D, G, H, 10A-C, E-H, K, L
chalcopyrite	$CuFeS_2$	massive; may fill late fractures in silicates and pyrrhotite	Figs. 6, 7A, B, D-G, I-L, 10A, B, E, G-J, L
Minor and trace ore minerals			
Fe-, Ni-bearing			
pyrite	FeS_2	intergrown with po, pn, and cp; symplectitic intergrowths with pn and cp	Figs. 7A, L, 10B, H
Ni-pyrite	$(Fe,Ni)S_2$	veins in po and pn	Fig. 7D, F, L
bravoite	$(Fe,Co,Ni)S_2$	rare; in fracture in po	
marcasite	FeS_2	flames in po or late veins in cp and po	Fig. 7E
troilite	FeS	exsolution lamellae in po and locally massive	Figs. 10C, F
magnetite	Fe_3O_4	euhedral inclusions in po or veins cutting po and cp; commonly associated with symplectitic textures at grain boundaries	Fig. 7F
argentopentlandite	$Ag(Fe,Ni)_8S_8$	exsolution lamellae and euhedral inclusions in cp	Figs. 7G and 10I
mackinawite	$(Fe,Ni)_{1+x}S$	exsolution lamellae in pn and rare cp	Figs. 7H and 10I
violarite	$FeNi_2S_4$	alteration of pn at rim or crystallographic interfaces	Fig. 7K
polydymite	$Ni_2+Ni_3+2S_4$	rare; alteration of pn associated with cp	
Cu-sulphides			
cubanite	$Cu_{23}FeS_4$	exsolution lamellae in cp and generally associated with tro-rich assemblages	Figs. 7I, 10I
geffroyite	$(Ag,Cu,Fe)_9(Se,S)_8$	rare; inclusion in cp	
Ni-arsenides			
gersdorffite-cobaltite	(Ni,Co)AsS	rare; euhedral intergrown with Pd-melonite, in pn	Fig. 10F
nickeline	NiAs	rare; inclusion in intergrown po-tro or at tip of cp grain	Fig. 10J
Pb-, Zn-sulphides			
galena	PbS	in fractures of gangue or rare inclusions in po, tro, and cp	
sphalerite	(Zn,Cd)S	rare; in cp	Figs. 7J
Bi-, Te-bearing			
hedleyite	$Bi_{2+x}Te_{1-x}$	rare; in silicate	
tellurobismuthite	Bi_2Te_3	rare; inclusion in po-pn, or at contact	
native tellurium	Te	rare; inclusions in po or pn and at sulphide-silicate interfaces	
native bismuth	Bi	rare; inclusions in po or pn and at sulphide-silicate interfaces	Fig. 10K
Ni-Bi sulphides			
parkerite	$Ni_3Bi_2S_2$	rare; at cp-silicate interfaces	Fig. 10I
Platinum group minerals			
merenskyite	$(Pd,Ni,Pt)(Te,Bi)_2$	most common PGM (3-23 μm); associated with po, pn, cp, py, and tro; inclusions in sulphides or occur at sulphide-sulphide or sulphide-silicate interfaces	Fig. 10A, B, L
moncheite	$(Pt,Pd)(Te,Bi)_2$	very common PGM (2-56 μm); inclusions in po, pn, cp, or silicate, or occur at sulphide-sulphide, sulphide-silicate interfaces, or in stringers (<160 μm) with cp and Ag-pn	Fig. 10D, E, G
palladian melonite	$(Pd,Ni)(Te,Bi)_2$	common; inclusions in po, pn, and tro (<30 μm)	Fig. 10C, F
froodite	$PdBi_2$	rare; satellite grain in silicate contacting cp	
sperrylite	$PtAs_2$	rare; inclusions (<50 μm) in cp or at cp-po-silicate interface	Fig. 10H
hollingworthite	RhAsS	rare; composite grain with Ni-merenskyite in cp-pn vein	Fig. 10L
Precious metal minerals			
hessite	Ag_2Te	most common PGM (3-8 μm); satellite grains in fractures in silicates, inclusions in cub, cp, pn, and silicate, at sulphide-sulphide or sulphide-silicate interfaces, or intergrown with moncheite	Fig. 10C, E, G
altaite	PbTe	rare; associated with cp	Fig. 10J

†Mineral chemistry is listed in Appendix G.

[1]Bold minerals indicate most abundant mineral in respective group.

[2]Mineral abbreviations: Ag-pn=argentopentlandite, cp=chalcopyrite, cub=cubanite, Pd-melonite=palladian melonite; PGM=platinum group mineral, pn=pentlandite, po=pyrrhotite, py=pyrite, tro=troilite.

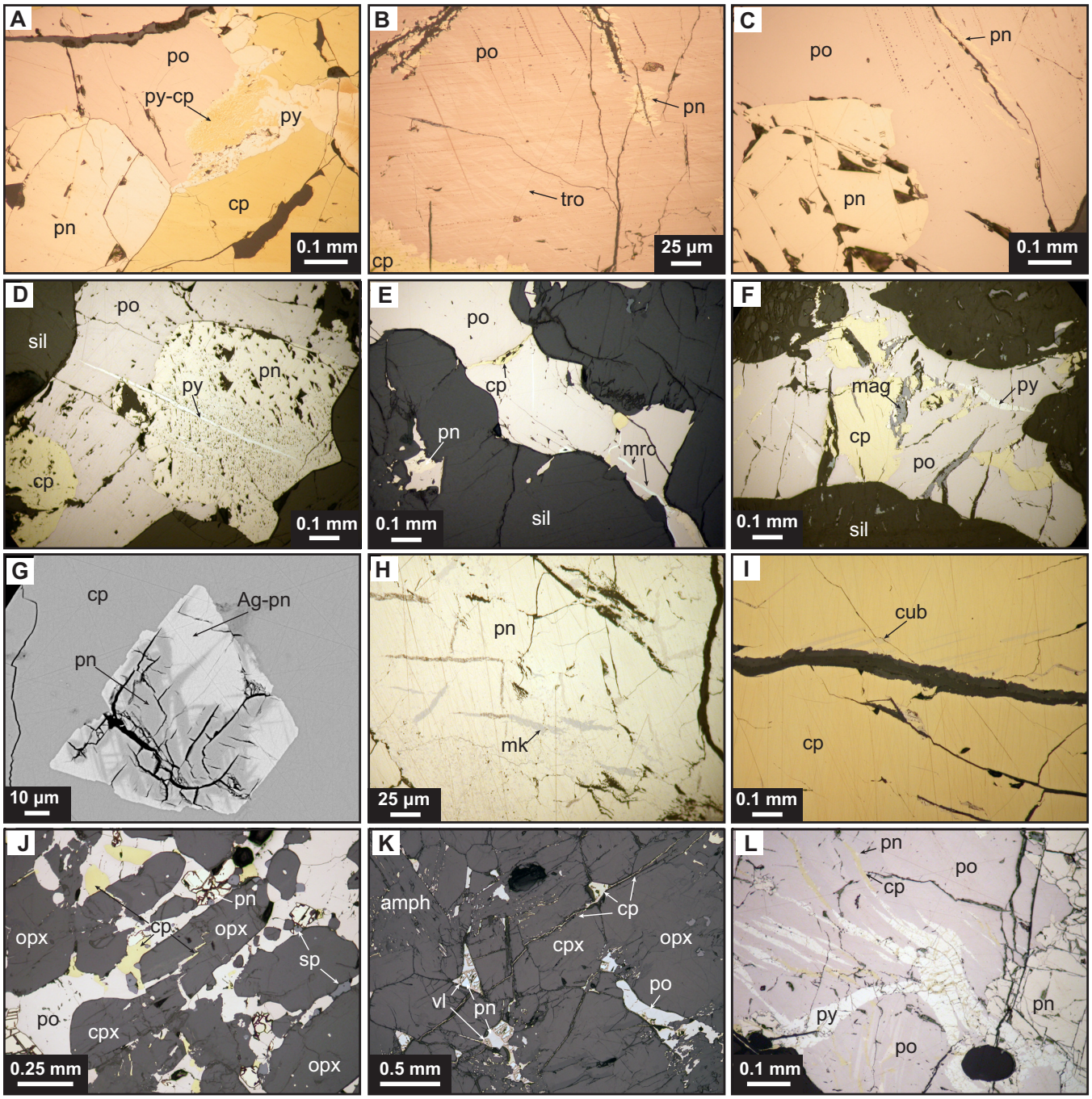

Figure 7. Photomicrographs and backscatter electron (BSE) images of sulphide textures in the Giant Mascot intrusion. **A)** Blocky pentlandite, massive chalcopyrite and pyrite, and symplectitic chalcopyrite-pyrite hosted by massive pyrrhotite (sample 71-EI-636). **B)** Troilite exsolution lamellae, pentlandite flames, and minor chalcopyrite in massive pyrrhotite (sample 12MMA-5-8-5A). **C)** Two forms of pentlandite — blocky grains and exsolution lamellae — hosted by massive pyrrhotite (sample 71-EI-615C). **D)** Blocky pentlandite, pyrite-pentlandite intergrowths, and chalcopyrite in pyrrhotite, with a pyrite vein cutting the intergrowths and pyrrhotite (sample 71-EI-634). **E)** Net-textured pyrrhotite containing chalcopyrite veins and marcasite flames (sample 71-EI-636). **F)** Pyrrhotite and chalcopyrite containing veins of pyrite and magnetite (sample M29-21). **G)** Argentopentlandite with pentlandite exsolution lamellae hosted by chalcopyrite (BSE) (sample 71-EI-624A). **H)** Massive pentlandite containing mackinawite [$(Fe,Ni)_{1+x}S$] exsolution lamellae (sample 12MMA-5-8-5A). **I)** Massive chalcopyrite containing cubanite exsolution lamellae (sample RHP01-078). **J)** Net-textured pyrrhotite, pentlandite, and chalcopyrite, with intergrown spinel and chalcopyrite-bearing fractures interstitial to orthopyroxene and clinopyroxene (sample 12MMA-5-8-1). **K)** Pyrrhotite and pentlandite (altered to violarite) interstitial to orthopyroxene, clinopyroxene, and amphibole; fractures in orthopyroxene and clinopyroxene are filled with chalcopyrite with evidence of localized microfaults (sample RHP01-109). **L)** Blocky pentlandite, veins of pyrite intergrown with chalcopyrite, and pentlandite exsolution lamellae at chalcopyrite grain boundaries, hosted in massive and strongly anisotropic pyrrhotite (sample RHP01-152). Mineral abbreviations: Ag-pn = argentopentlandite; amph = amphibole; cp = chalcopyrite; cpx = clinopyroxene; cub = cubanite; mag = magnetite; mk = mackinawite; mrc = marcasite; opx = orthopyroxene; pn = pentlandite; po = pyrrhotite; py = pyrite; sil = silicate; sp = sphalerite; tro = troilite; vl = violarite.

nated from the sulphide melt by orthomagmatic processes with no hydrothermal input. The final step, to determine the proportions of non-sulphide, was to account for significant Ni contents in olivine in the Giant Mascot ores. Naldrett et al. (2000) calculated the Ni/Fe ratio in sulphide and assumed a constant 25% modal proportion of olivine in each sample. Tests introducing actual modal percentages and Ni concentrations of olivine in each sample indicate that there is no significant shift in the data and that the calculation procedure used previously is robust. The amount of Ni attributed to olivine was then used to recalculate the raw Ni content in sulphide and to achieve a final Ni tenor.

Sulphide mineral compositions

The mineral chemistry for the sulphide and platinum group minerals are reported in Appendix F. The predominant base metal sulphide minerals, present in all ores of the Giant Mascot deposit, are pyrrhotite, pentlandite, chalcopyrite, and minor pyrite (Tables 3 and 4). Of the Fe-Ni sulphide minerals, pyrrhotite is the most abundant (Figs. 6, 7) and is present as both magnetic monoclinic (Fe_7S_8) and non-magnetic hexagonal (e.g. $Fe_{11}S_{12}$) varieties (e.g. Becker et al., 2010) (Figs. 6, 7, 8). Pyrrhotite compositions (n=61) range from $Fe_{52.7}S_{38.0}$ to $Fe_{62.3}S_{38.6}$ (average=$Fe_{60.2}Ni_{0.71}S_{39.0}$) and contain up to 1.10 wt% Ni (Fig. 9; Appendix G). Coexisting troilite (n=11) compositions are nearly stoichiometric ($Fe_{1.02}S$) with a restricted range of Fe contents characteristically higher than in pyrrhotite (62.9–64.5 wt%; Fig. 9). Pentlandite has an average composition of $(Ni_{4.7}Fe_{4.4}Co_{0.1})_{\Sigma 9.2}S_8$ (n=64) with up to 3.52 wt% Co and 0.08 wt% Ag, whereas argentopentlandite is invariably found in chalcopyrite and contains 11.8 to 12.3 wt% Ag with an average composition of $Ag_{12.1}(Ni_{18.9}Fe_{37.4}Co_{0.01})S_{31.6}$ (n=3; Fig. 9A). Violarite (Fig. 7K), polydymite, and symplectitic intergrowths of pyrrhotite-orthopyroxene, chalcopyrite-chlorite+actinolite, and pyrite-chalcopyrite (Fig. 7A) are interpreted as low-temperature or late post-ore metamorphic products of pentlandite.

Chalcopyrite compositions do not vary with texture (i.e. massive versus veins), are stoichiometric, and average $Cu_{1.02}Fe_{1.03}S_2$ (n=31; Figs. 6, 7E, F). Pyrite shows minimal variation in Fe content (average= $[Fe_{0.97}Co_{0.03}]S_2$; n=36) (Fig. 9A); however, massive pyrite (Figs. 7A, L, 10B) has distinctly lower Ni contents (0–0.1 wt%) compared to secondary pyrite veins (0.12–0.54 wt%; Figs. 7D, F, L, 10H), with an anomalous pyrite-pentlandite symplectite yielding the highest Ni contents (3.92 wt%). Secondary pyrite veins also contain 0.7 to 3.08 wt% Co, which chemically distinguishes them from secondary marcasite flames and veins (0.02–0.65 wt%) (Appendix G).

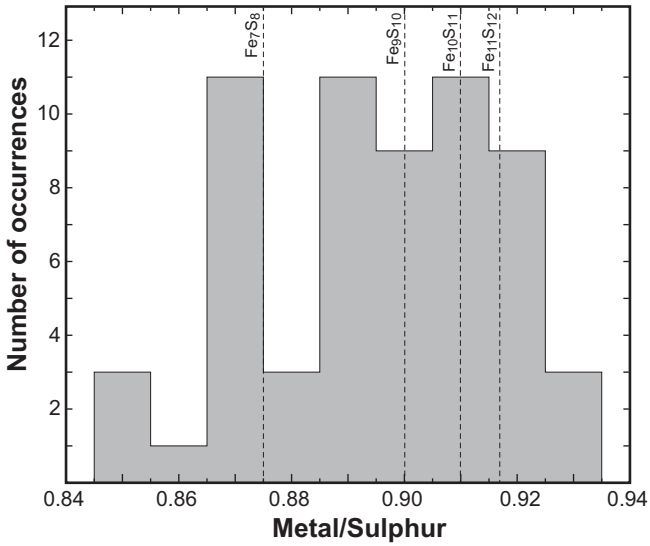

Figure 8. Atomic metal/sulphur ratios for EMPA analyses of pyrrhotite from the Giant Mascot Ni-Cu-PGE deposit. Superimposed dashed lines indicate fields of varying pyrrhotite compositions (after Becker et al., 2010).

Platinum group minerals and associated sulpharsenide minerals

Prior to this study, the concentration of platinum group elements in Giant Mascot ores was unknown. Here we present a summary of the platinum group minerals (PGM) in the Giant Mascot Ni-Cu-PGE deposit. Sulpharsenide minerals, such as gersdorffite (NiAsS), cobaltite (CoAsS), and nickeline (NiAs) are typically associated with platinum group minerals or precious metal minerals (PMM) (Fig. 10F, J). Most of the PGMs identified are telluride or bismuthotelluride, predominantly merenskyite ($PdTe_2$), moncheite ($PtTe_2$), and melonite ($NiTe_2$) (Table 4; Fig. 11A, B; Appendix G2). The PGMs are mostly associated with pentlandite (Figs. 10B, C, F; 11C) and other base metal sulphide minerals. Generally, PGMs may be fully enclosed in sulphide, at sulphide-sulphide or sulphide-silicate interfaces, in sulphide veins in other sulphides or less commonly in silicate minerals and as satellite grains in fractured silicate. Merenskyite and moncheite are the most common PGMs in the Giant Mascot deposit. Merenskyite occurs as three compositional varieties: Pt-rich, Ni-rich, and near-stoichiometric merenskyite (Figs. 10A,B, 11A). Moncheite is present as either stoichiometric or Pd-rich compositions (Figs. 10D, E, 11A); the Pd-rich variety has an average composition of $[(Pt_{0.35}Pd_{0.31})(Te_{1.87}Bi_{0.14})]$ (n=3). Palladian melonite is less abundant, but common, and has an average composition of $[(Ni_{0.84}Pd_{0.23})(Te_{1.87}Bi_{0.13})]$ (n=11; Fig. 10C, F). As-bearing PGMs (i.e. sperrylite and hollingworthite) are rare and associated with chalcopyrite (Fig. 10H, L). Precious metal minerals are typically tellurides, but form ligands with Ag (e.g. hessite), and

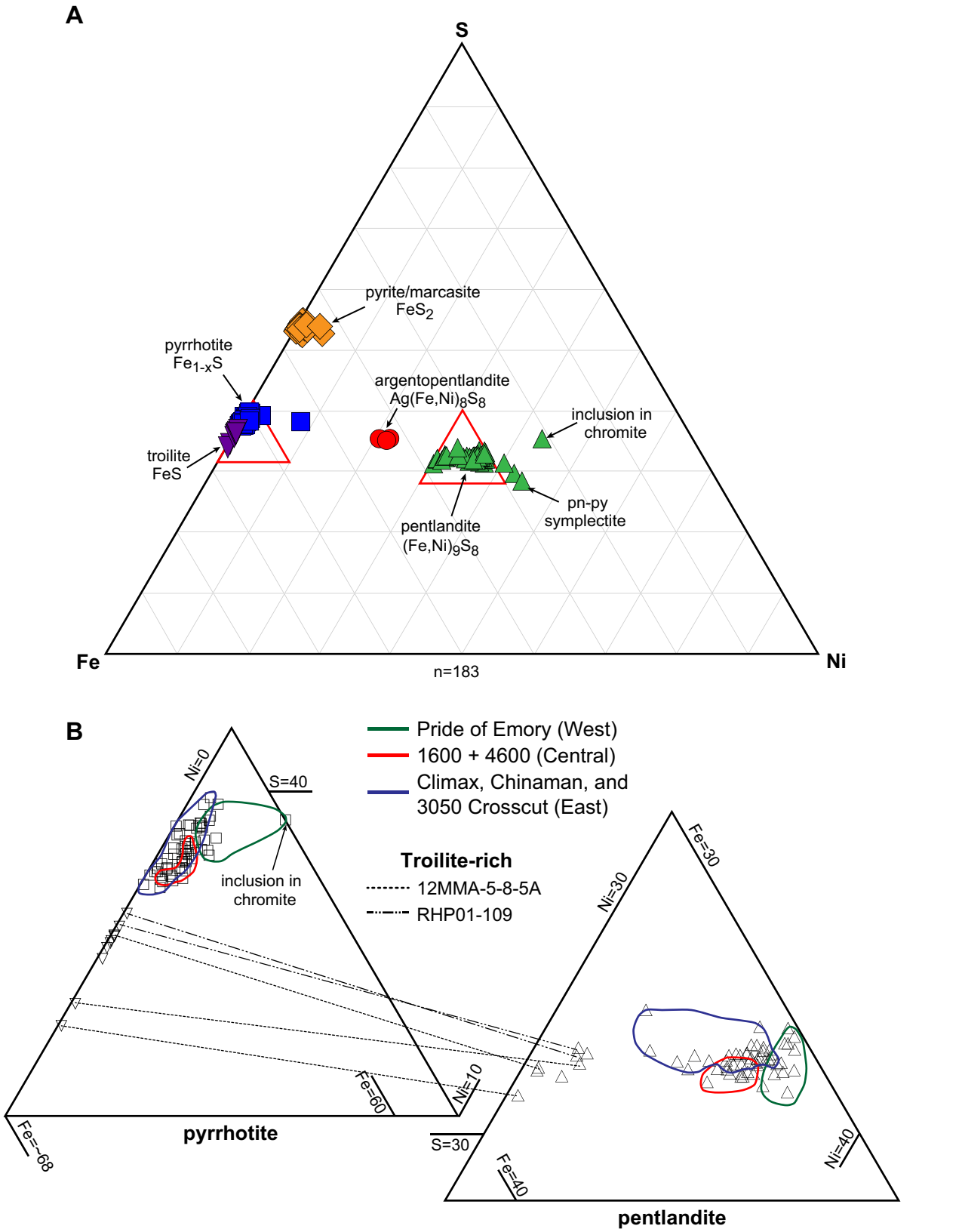

Figure 9. Ternary plots of the compositions of Fe-, Ni-, and S-bearing base metal sulphides in the Giant Mascot Ni-Cu-PGE deposit. **A)** Ternary diagram showing the characteristic compositions of pyrrhotite, pentlandite, argentopentlandite, pyrite, and troilite. **B)** Two areas of the above ternary diagram (outlined in red) are enlarged for pyrrhotite and troilite (left) and pentlandite (right). Coloured lines enclose mineral compositions observed in each mineralization zone. Note the most Fe-rich and Ni-poor pentlandites (indicated by dotted and dashed tie lines) are associated with troilite. Analyses are EMPA results in weight percent normalized to 100%.

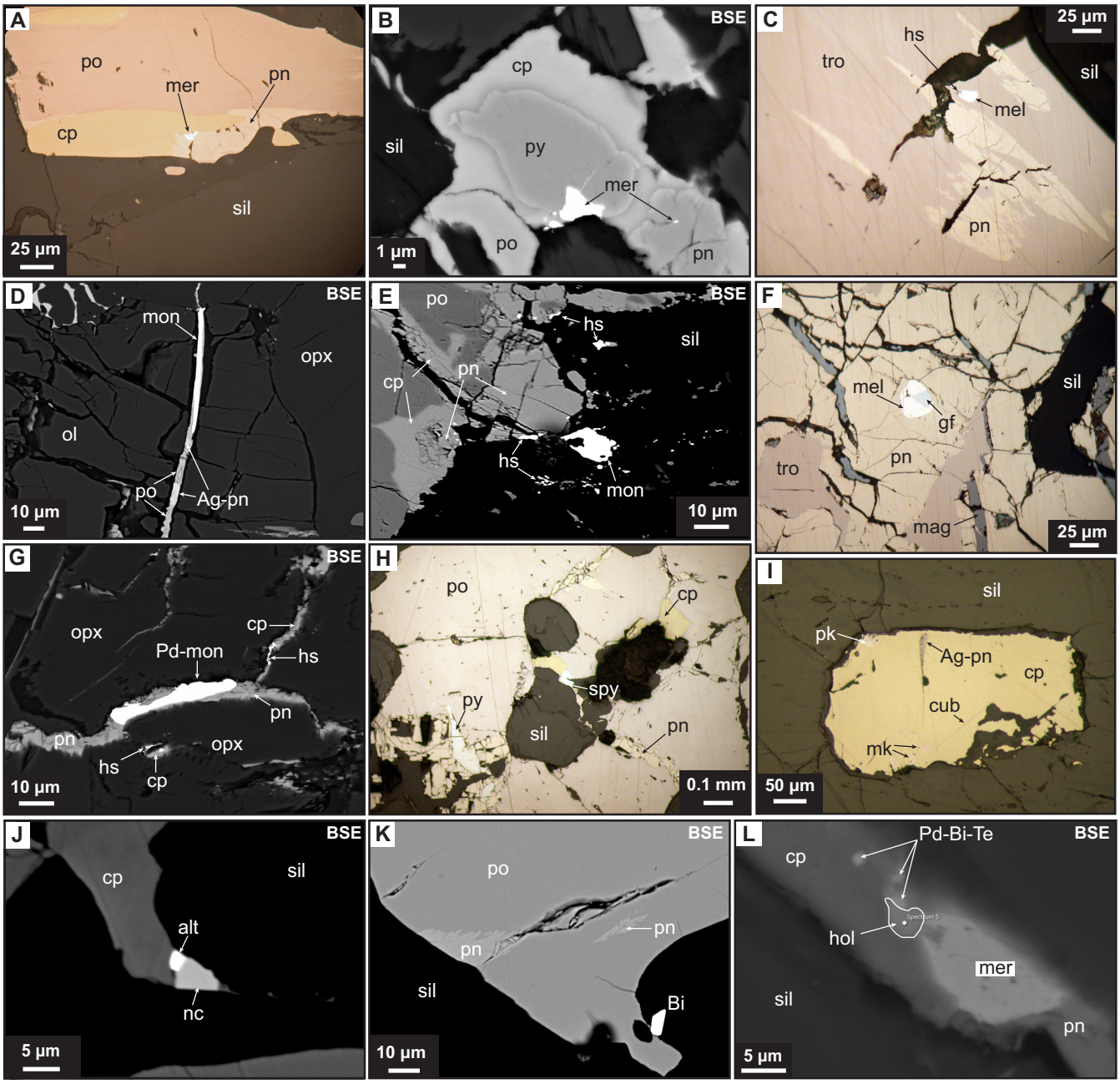

Figure 10. Photomicrographs and backscatter electron (BSE) images of platinum-group and precious-metal minerals in Giant Mascot ores. **A)** Bright white anhedral merenskyite hosted by pentlandite at the grain boundary of chalcopyrite, both within pyrrhotite (sample 71-EI-615A). **B)** Merenskyite hosted in pyrite and chalcopyrite, and associated with pyrrhotite and pentlandite (BSE) (sample 179-E-847). **C)** Bright white, anhedral palladian melonite tipped by hessite and fully enclosed in troilite proximal to pentlandite flames (sample 12MMA-5-8-5A). **D)** Moncheite hosted by a chalcopyrite and argentopentlandite compound vein within fractured olivine (BSE) (sample RHP01-078). **E)** Moncheite fully enclosed by silicates, a smaller elongate moncheite at the boundary of pentlandite and silicate, and small satellite grains of hessite that are fully enclosed in silicates along silicate-sulphide boundaries (BSE) (sample RHP01-152). **F)** Bright white, anhedral palladian melonite intergrown with euhedral gersdorffite, which are hosted by pentlandite that contains magnetite veins, and surrounded by troilite (sample 12MMA-5-8-5A). **G)** Palladian moncheite in a pentlandite vein, and hessite in chalcopyrite veins in orthopyroxene (sample RHP01-078). **H)** Bright white sperrylite at the boundary of chalcopyrite and pyrrhotite; blocky pentlandite and pentlandite flames proximal to pyrite (sample 71-EI-657). **I)** Cream-coloured parkerite enclosed in chalcopyrite, which contains argentopentlandite, mackinawite, and cubanite flames (sample RHP01-109). **J)** Altaite in contact with chalcopyrite, nickeline, and silicates (BSE) (sample RHP01-109). **K)** A euhedral bismuth grain in contact with silicate and pyrrhotite, which contains pentlandite flames (sample 179-E-847). **L)** Intergrown merenskyite, hollingworthite, and other Pd-Bi tellurides in a composite vein of chalcopyrite and pentlandite in silicate (sample 71-EI-615A). Mineral abbreviations as in Figure 7, except: alt = altaite; Bi = bismuth; cub = cubanite; ger = gersdorffite; gf = gersdorffite; hol = hollingworthite; hs = hessite; mag = magnetite; mel = palladian melonite; mer = merenskyite; mk = mackinawite; mon = moncheite; nc = nickeline; ol = olivine; opx = orthopyroxene; Pd-mon = palladian moncheite; pk = parkerite; sil = silicate; spy = sperrylite; Te = telluride; tro = troilite. Refer to Table 4 for additional textural descriptions.

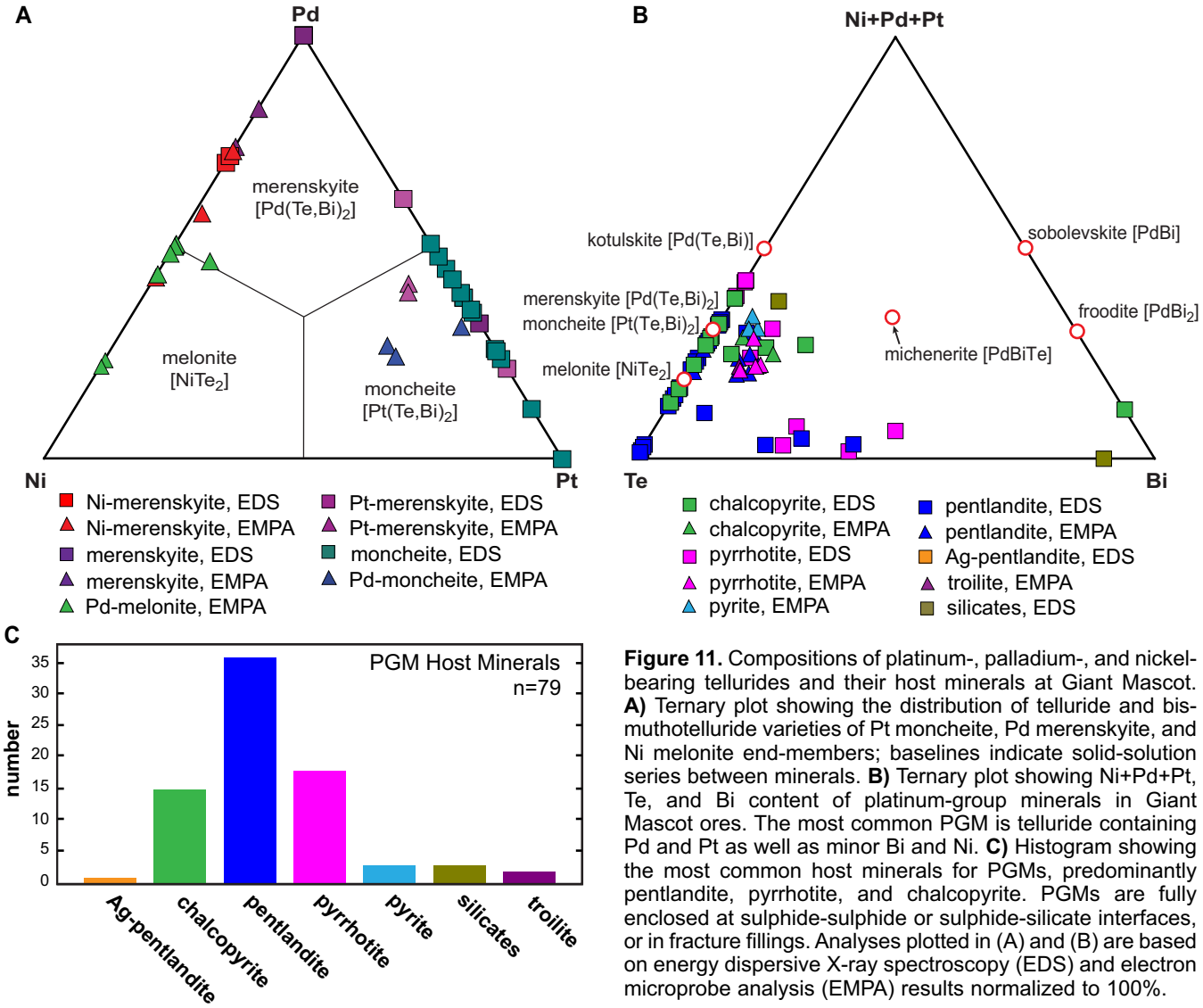

Figure 11. Compositions of platinum-, palladium-, and nickel-bearing tellurides and their host minerals at Giant Mascot. **A)** Ternary plot showing the distribution of telluride and bismuthotelluride varieties of Pt moncheite, Pd merenskyite, and Ni melonite end-members; baselines indicate solid-solution series between minerals. **B)** Ternary plot showing Ni+Pd+Pt, Te, and Bi content of platinum-group minerals in Giant Mascot ores. The most common PGM is telluride containing Pd and Pt as well as minor Bi and Ni. **C)** Histogram showing the most common host minerals for PGMs, predominantly pentlandite, pyrrhotite, and chalcopyrite. PGMs are fully enclosed at sulphide-sulphide or sulphide-silicate interfaces, or in fracture fillings. Analyses plotted in (A) and (B) are based on energy dispersive X-ray spectroscopy (EDS) and electron microprobe analysis (EMPA) results normalized to 100%.

less commonly with Pb (e.g. altaite) (Table 4; Fig. 10E, G, J).

SUMMARY

This report is a database release that supports the ongoing study to create a classification for magmatic Ni-Cu-PGE sulphide deposits hosted by ultramafic-mafic intrusions in convergent margin tectonic settings. The two mineralized ultramafic intrusions in the Cordillera that were investigated to determine the ore-forming characteristics and mode of occurrence of Ni-Cu-PGE mineralization include (1) the orthopyroxene-absent Turnagain Alaskan-type, and (2) the orthopyroxene-rich Giant Mascot intrusions. Knowledge gained from this study will aid in the development of practical exploration criteria for the Canadian Cordillera and other convergent margin environments globally.

ACKNOWLEDGEMENTS

We thank Dr. Mati Raudsepp, Edith Czech, Elisabetta Pani, Jenny Lai, and Lan Kato (UBC), and Patricia Hunt (GSC-Ottawa) for training and guidance with SEM and EMPA analyses, and Ingrid Kjarsgaard (Ottawa) for petrographic and EMPA work on sulphides and platinum group minerals. Dr. Marg Amini and Corey Wall are also acknowledged for guidance on analyses with the laser ablation ICP-MS instruments at PCIGR (UBC). The senior author was supported by the NRCan Research Affiliate Program (RAP). Additional funds were supplied by a Society of Economic Geology-Canada Foundation Graduate Student Research Grant awarded to Matthew Manor in 2013.

REFERENCES

Aho, A.E., 1954. Geology and ore deposits of the property of Pacific Nickel Mines near Hope, British Columbia; Ph.D. Thesis, University of California Santa Barbara, Santa Barbara, California, 158 p.

Aho, A.E., 1956. Geology and genesis of ultrabasic nickel-copper-pyrrhotite deposits at the Pacific Nickel Property, southwestern British Columbia; Economic Geology, v. 51, p. 441–481.

Ames, D.E. and Houlé, M.G., 2011. Overview of the Targeted Geoscience Initiative 4 Nickel-Copper-Platinum Group Elements-Chromium Project (2010–2015)—Mafic to ultramafic ore systems: Footprint, fertility and vectors; Summary of Field Work and Other Activities 2011, Ontario Geological Survey Open File Report 6270, p. 37-1 to 37-7.

Amirault, F. and Burnham, O.M., 2013. Carbon and sulphur analysis in geological samples by combustion-infrared: Verifying method capabilities on new instrumentation; Summary of Fieldwork and Other Activities 2013, Ontario Geological Survey Open File Report 6290, p. 43-1 to 43-5.

Becker, M., de Villiers, J., and Bradshaw, D., 2010. The mineralogy and crystallography of pyrrhotite from selected nickel and PGE ore deposits; Economic Geology, v. 105, p. 1025–1037.

Black, L.P., Kamo, S.L., Allen, C.M., Davis, D.W., Aleinikoff, J.N., Valley, J.W., Mundil, R., Campbell, I.H., Korsch, R.J., Williams, I.S., and Foudoulis, C., 2004. Improved $^{206}Pb/^{238}U$ microprobe geochronology by the monitoring of a trace-element-related matrix effect; SHRIMP, ID-TIMS, ELA-ICP-MS and oxygen isotope documentation for a series of zircon standards; Chemical Geology, v. 205, p. 115–140.

Brown, E.H. and McClelland, W.C., 2000. Pluton emplacement by sheeting and vertical ballooning in part of the southeast Coast Plutonic Complex, British Columbia; Geological Society of America Bulletin, v. 112, p. 708–719.

Brown, E.H. and Walker, N.W., 1993. A magma-loading model for Barrovian metamorphism in the southeast Coast Plutonic Complex, British Columbia and Washington; Geological Society of America Bulletin, v. 105, p. 479–500.

Brown, E.H., Talbot, J.L., McClelland, W.C., Feltman, J.A., Lapen, T.J., Bennett, J.D., Hettinga, M.A., Troost, M.L., Alvarez, K.M., and Calvert, A.T., 2000. Interplay of plutonism and regional deformation in an obliquely convergent arc, southern Coast Belt, British Columbia; Tectonics, v. 19, p. 493–511.

Christopher, P.A. and Robinson, J.W., 1975. Pride of Emory Mine (92H/SW-4), *In:* Exploration and Mining in British Columbia 1974; British Columbia Ministry of Mines and Petroleum Resources, p. 105–113.

Clarke, W.E., 1969. Giant Mascot Mines Ltd., Geology and ore controls; Western Miner, v. 42, p. 40–46.

Colpron, M. and Nelson, J.L., 2011. A digital atlas of terranes for the Northern Cordillera; British Columbia Ministry of Energy and Mines, BCGS GeoFile 2011-11.

Eggins, S.M., Kinsley, L.P.J., and Shelley, J.M.G., 1998. Deposition and element fractionation processes during atmospheric pressure laser sampling for analysis by ICP-MS; Applied Surface Science, v. 127, p. 278–286.

Ferry, J.M. and Watson, E.B., 2007. New thermodynamic models and revised calibrations for the Ti-in-zircon and Zr-in-rutile thermometers; Contributions to Mineralogy and Petrology, v. 154, p. 429–437.

Gabites, J.E., 1985. Geology and geochronometry of the Cogburn Creek-Settler Creek area, northeast of Harrison Lake, B.C.; M.Sc. Thesis, University of British Columbia, Vancouver, British Columbia, 153 p.

Gao, J.-F., Zhou, M.-F., Lightfoot, P.C., Wang, C.Y., Qi, L., and Sun, M., 2013. Sulfide saturation and magma emplacement in the formation of the Permian Huangshandong Ni-Cu sulfide deposit, Xinjiang, Northwestern China; Economic Geology, v. 108, p. 1833–1848.

Gehrels, G., Rusmore, M., Woodsworth, G., Crawford, M., Andronicos, C., Hollister, L., Patchett, J., Ducea, M., Butler, R., Klepeis, K., Davidson, C., Friedman, R., Haggart, J., Mahoney, B., Crawford, W., Pearson, D., and Girardi, J., 2009. U-Th-Pb geochronology of the Coast Mountains batholith in north-coastal British Columbia: Constraints on age and tectonic evolution; Geological Society of America Bulletin, v. 121, p. 1341–1361.

Gromet, L.P. and Silver, L.T., 1983. Rare earth element distributions among minerals in a granodiorite and their petrogenetic implications; Geochimica et Cosmochimica Acta, v. 47, p. 925–939.

Hulbert, L.J., 2001. GIS maps and databases of mafic-ultramafic hosted Ni, Ni-Cu, Cr +/- PGE occurrences and mafic-ultramafic bodies in British Columbia; British Columbia Ministry of Energy and Mines, Geoscience Map 2001-2.

Jackson, S.E., Fryer, B.J., Gosse, W., Healey, D.C., Longerich, H.P., and Strong, D.F., 1990. Determination of the precious metals in geological materials by inductively coupled plasma-mass spectrometry (ICP-MS) with nickel sulphide fire-assay collection and tellurium coprecipitation; Chemical Geology, v. 83, p. 119–132.

Kerr, A., 2003. Guidelines for the calculation and use of sulphide metal contents in research and mineral exploration, In: Current Research; Newfoundland Geological Survey, Report 03-1, p. 223–229.

Manor, M.J., 2014. Convergent margin Ni-Cu-PGE deposits: Geology, geochronology, and geochemistry of the Giant Mascot magmatic sulphide deposit, Hope, British Columbia; M.Sc. Thesis, University of British Columbia, Vancouver, British Columbia, 371 p.

Manor, M.J., Wall, C.J., Nixon, G.T., Scoates, J.S., Pinsent, R.H., and Ames, D.E., 2014. Preliminary geology and geochemistry of the Giant Mascot ultramafic-mafic intrusion, Hope, southwestern British Columbia; Geological Survey of Canada, Open File 7570 (British Columbia Ministry of Energy and Mines, Open File 2014-03); scale 1:10 000.

Manor, M.J., Wall, C.J., Friedman, R.M., Gabites, J., Nixon, G.T., Scoates, J.S., and Ames, D.E., 2015. Geology, geochronology and Ni-Cu-PGE orebodies of the Giant Mascot ultramafic intrusion, Hope, southwestern British Columbia; Geological Survey of Canada, Open File 7767 (British Columbia Ministry of Energy and Mines, Open File 2015-01), scale 1:10 000. 2 sheets.

McDonough, W. and Sun, S., 1995. The composition of the Earth; Chemical Geology, v. 120, p. 223–253.

McLeod, J.A., 1975. The Giant Mascot ultramafite and its related ores; M.Sc. Thesis, University of British Columbia, Vancouver, British Columbia, 136 p.

Mitrovic, I., 2013. Evolution of the Coast Cascade Orogen by tectonic thickening and magmatic loading: The Cretaceous Breakenridge complex, southwestern British Columbia; M.Sc. Thesis, Simon Fraser University, Vancouver, British Columbia, 133 p.

Monger, J.W.H., 1989. Geology, Hope, British Columbia; Geological Survey of Canada, Map 41-1989, Sheet 1, scale 1:250,000.

Naldrett, A.J., 2011. Fundamentals of magmatic sulfide deposits; Reviews in Economic Geology, v. 17, p. 1–50.

Naldrett, A.J., Asif, M., Krstic, S., and Li, C., 2000. The composition of mineralization at the Voisey's Bay Ni-Cu sulfide deposit, with special reference to platinum-group elements; Economic Geology, v. 95, p. 845–865.

Norrish, K. and Hutton, J.T., 1969. An accurate X-ray spectrographic method for the analysis of a wide range of geological samples; Geochimica et Cosmochimica Acta, v. 33, p. 431–453.

Paton, C., Hellstrom, J., Bence, P., Woodhead, J., and Hergt, J., 2011. Iolite: Freeware for the visualization and processing of mass spectrometric data; Journal of Analytical Atomic Spectrometry, v. 26, p. 2508–2518.

Pearce, J.A., Baker, P.E., Harvey, P.K., and Luff, I.W., 1995. Geochemical evidence for subduction fluxes, mantle melting

and fractional crystallization beneath the south Sandwich island arc; Journal of Petrology, v. 36, p. 1073–1109.

Pigage, L.C., 1973. Metamorphism southwest of Yale, British Columbia; M.Sc. Thesis, University of British Columbia, Vancouver, British Columbia, 114 p.

Piña, R., Gervilla, F., Ortega, L., and Lunar, R., 2008. Mineralogy and geochemistry of platinum-group elements in the Aguablanca Ni-Cu deposit (SW Spain); Mineralogy and Petrology, v. 92, p. 259–282.

Pouchou, J.-L. and Pichoir, F., 1991. Quantitative analysis of homogeneous or stratified microvolumes applying the model "PAP", *In:* Electron Probe Quantitation, (ed.) K.F.J. Heinrich and D.E. Newbury; Springer, p. 31–75.

Reiners, P.W., Ehlers, T.A., Garver, J.I., Mitchell, S.G., Montgomery, D.R., Vance, J.A., and Nicolescu, S., 2002. Late Miocene exhumation and uplift of the Washington Cascade Range; Geology, v. 30, p. 767–770.

Richards, T.A., 1971. Plutonic rocks between Hope, B.C. and the 49th Parallel; Ph.D. Thesis, University of British Columbia, Vancouver, British Columbia, 193 p.

Richards, T.A. and McTaggart, K.C., 1976. Granitic rocks of the southern Coast Plutonic Complex and northern Cascades of British Columbia; Geological Society of America Bulletin, v. 87, p. 935–953.

Richardson, T. and Burnham, O.M., 2002. Precious metal analysis at the Geoscience Laboratories: Results from the new low-level analytical facility, *In:* Summary of Fieldwork and Other Activities 2013; Ontario Geological Survey, Open File Report 6100, p. 35-1 to 35-5.

Ripley, E.M., 2010. A new perspective on exploration for magmatic sulfide-rich Ni-Cu-(PGE) deposits, Chapter 24 *In:* The Challenge of Finding New Mineral Resources: Global Metallogeny, Innovation Exploration, and New Discoveries; (ed.) R.J. Goldfarb, E.E. Marsh, and T. Monecke); Society of Economic Geologists, Special Publication No. 15, v. II, p. 437–450.

Sappin, A.-A., Constantin, M., and Clark, T., 2012. Petrology of mafic and ultramafic intrusions from the Portneuf-Mauricie Domain, Grenville Province, Canada: Implications for plutonic complexes in a Proterozoic island arc; Lithos, v. 154, p. 277–295.

Shazali, I., Van't Dack, L., and Gijbels, R., 1987. Determination of precious metals in ores and rocks by thermal neutron activation/γ-spectrometry after preconcentration by nickel sulphide fire assay and coprecipitation with tellurium; Analytica Chimica Acta, v. 196, p. 49–58.

Sláma, J., Košler, J., Condon, D.J., Crowley, J.L., Gerdes, A., Hanchar, J.M., Horstwood, M.S.A., Morris, G.A., Nasdala, L., Norberg, N., Schaltegger, U., Schoene, B., Tubrett, M.N., and Whitehouse, M.J., 2008. Plešovice zircon – A new natural reference material for U-Pb and Hf isotopic microanalysis; Chemical Geology, v. 249, p. 1–35.

Vining, M.R., 1977. The Spuzzum pluton northwest of Hope, B.C.; M.Sc. Thesis, University of British Columbia, Vancouver, British Columbia, 159 p.